

박사학위논문

Ph.D. Dissertation

변형률 완화 다각형 유한요소 개발 및
변형률 완화 요소법에서의 체적 잠김 개선

Development of strain-smoothed polygonal finite elements
and alleviation of volumetric locking in the strain-smoothed
element method

2024

정훈태 (鄭勳兌 Jung, Hoontae)

한국과학기술원

Korea Advanced Institute of Science and Technology

박 사 학 위 논 문

변형률 완화 다각형 유한요소 개발 및
변형률 완화 요소법에서의 체적 잠김 개선

2024

정 훈 태

한 국 과 학 기 술 원

기계공학부

변형률 완화 다각형 유한요소 개발 및
변형률 완화 요소법에서의 체적 잠김 개선

정 훈 태

위 논문은 한국과학기술원 박사학위논문으로
학위논문 심사위원회의 심사를 통과하였음

2023년 12월 15일

심사위원장 이 필 승 (인)

심사위원 유 승 화 (인)

심사위원 윤 정 환 (인)

심사위원 장 대 준 (인)

심사위원 전 형 민 (인)

Development of strain-smoothed polygonal finite elements and alleviation of volumetric locking in the strain-smoothed element method

Hoontae Jung

Advisor: Phill-Seung Lee

A dissertation/thesis submitted to the faculty of
Korea Advanced Institute of Science and Technology in
partial fulfillment of the requirements for the degree of
Doctor of Philosophy in Mechanical Engineering

Daejeon, Korea
December 15, 2023

Approved by

Phill-Seung Lee
Professor of Mechanical Engineering

The study was conducted in accordance with Code of Research Ethics¹⁾.

1) Declaration of Ethical Conduct in Research: I, as a graduate student of Korea Advanced Institute of Science and Technology, hereby declare that I have not committed any act that may damage the credibility of my research. This includes, but is not limited to, falsification, thesis written by someone else, distortion of research findings, and plagiarism. I confirm that my dissertation contains honest conclusions based on my own careful research under the guidance of my advisor.

DME

정훈태. 변형률 완화 다각형 유한요소 개발 및 변형률 완화 요소법에서의 체적 잠김 개선. 기계공학과. 2024년. 63+v 쪽.
지도교수: 이필승.(영문 논문)

Hoontae Jung. Development of strain-smoothed polygonal finite elements and alleviation of volumetric locking in the strain-smoothed element method. Department of Mechanical Engineering. 2024. 63+v pages. Advisor: Phill-Seung Lee. (Text in English)

초 록

본 학위 논문에서는 변형률 완화 요소법(strain-smoothed element method; SSE method)을 적용한 다각형 유한 요소를 제안하고, 변형률 완화 요소법이 적용된 3절점 삼각 요소에서의 체적 잠김을 개선하는 방안을 제안하고자 한다. 변형률 완화 요소법은 평활화된 변형률을 기반으로 별도의 평활 도메인 없이 요소 내에 선형의 변형률장을 구성하며, 삼각형 및 사각형 요소에 적용되어 많은 성능 개선을 이루었다. 다각형 요소는 격자 생성의 유연성 등의 이점이 있어 여러 활용방안이 모색되어왔으나 공학 문제에서의 활용을 위해서는 요소의 성능 개선이 여전히 필요하며, 변형률 완화 요소법(SSE)을 이용하여 개선된 다각형 유한요소를 제안하고자 한다. SSE 기법을 다각형 요소에 적용하기 위하여, 요소의 삼각분할을 통한 부분 선형 형상함수(piecewise linear shape function)가 이용되며 각 요소를 단위로 평활화된 변형률장이 구성된다. 또한 비압축성에 가까운 재료의 해석 시 체적 잠김이 발생하는데, 3절점 삼각 요소의 경우 보간 함수의 차수가 낮아 이를 완화하는데 어려움이 있으며, 평활화가 적용된 변형률 완화 3절점 삼각 요소 또한 체적 잠김 개선에 어려움이 있었다. 본 연구에서는 요소의 적분점들에 할당되어 있던 변형률로부터 절점에서의 평활화된 체적 변형률을 새로 정의하고, 절점에서의 체적 변형률로부터 요소 내의 체적 변형률장을 구성한다. 제안하는 요소의 성능을 검증하기 위하여 다양한 수치 예제에서의 수렴 거동을 관찰하였다.

핵 심 낱 말 유한요소해석, 변형률 완화 요소법, 솔리드 요소, 삼각형 요소, 다각형 요소, 체적 잠김

Abstract

Herein, we present effective polygonal finite elements to which the strain-smoothed element (SSE) method is applied. Recently, the SSE method has been developed for conventional triangular and quadrilateral finite elements; furthermore, it has been shown to improve the performance of finite elements. Polygonal elements enable various applications through flexible mesh handling; however, further development is still required to use them more effectively in engineering practice. In this study, piecewise linear shape functions are adopted, the SSE method is applied through the triangulation of polygonal elements, and a smoothed strain field is constructed within the element. In addition, volumetric locking occurs when analyzing materials that are close to incompressible. In the case of 3-node triangular element, the lower order of interpolation functions makes it challenging to alleviate the locking. Furthermore, the 3-node strain-smoothed element is also facing difficulties in alleviating volumetric locking. In this study, a new definition of the smoothed volumetric strain at the nodal points is derived from the strains assigned at the integration points, and the volumetric strain field within the element is formed from the nodal smoothed volumetric strains. The strain-smoothed polygonal elements and the strain-smoothed 3-node triangular element with volumetric locking alleviation pass basic tests and show improved convergence behaviors in various numerical problems.

Keywords Finite element analysis, Strain-smoothed element method, Solid elements, Triangular elements, Polygonal elements, Volumetric locking

Contents

| | |
|---|-----|
| Contents | i |
| List of Tables | ii |
| List of Figures | iii |
| Chapter 1. Introduction | 1 |
| Chapter 2. Strain-smoothed polygonal finite elements | 3 |
| 2.1 Strain-smoothed element method for 2D solid elements | 3 |
| 2.2 Formulation of the strain-smoothed polygonal finite element | 6 |
| 2.2.1 Integration of polygonal elements | 6 |
| 2.2.2 Geometry and displacement interpolations | 7 |
| 2.2.3 Strain smoothing | 8 |
| 2.2.4 Strain-displacement relation and stiffness matrix..... | 12 |
| 2.3 Basic numerical tests | 14 |
| 2.4 Numerical examples | 17 |
| 2.4.1 Infinite plate with a circular hole | 17 |
| 2.4.2 Cook's skew beam | 18 |
| 2.4.3 Dam problem | 19 |
| 2.4.4 Ring problem | 20 |
| Chapter 3. Volumetric locking alleviation in the strain-smoothed 3-node triangular finite element | 36 |
| 3.1 Volumetric locking in 2D solid elements | 37 |
| 3.1.1 Treatment of volumetric locking in the strain-smoothed elements | 39 |
| 3.2 Formulation of the strain-smoothed 3-node triangular finite element to alleviate volumetric locking | 42 |
| 3.2.1 Strain-smoothed element method for deviatoric strain | 42 |
| 3.2.2 Smoothed volumetric strain by strain-smoothed element method | 43 |
| 3.3 Basic numerical tests | 47 |
| 3.4 Numerical examples | 48 |
| 3.4.1 Square block problem | 49 |
| 3.4.2 Infinite plate with a circular hole | 52 |
| 3.4.3 Cook's skew beam | 54 |
| 3.4.4 Dam problem | 57 |
| Chapter 4. Concluding Remark | 60 |
| Bibliography | 61 |

List of Tables

| | |
|--|----|
| Table 2.1. Minimum and maximum stress values for all Gauss integration points in the patch tests (minimum stress/maximum stress). | 15 |
| Table 2.2. Relative errors in the horizontal displacement ($ u_{\text{ref}} - u_h /u_{\text{ref}} \times 100$) at point A in the infinite plate with a circular hole. | 21 |
| Table 2.3. Relative errors in the vertical displacement ($ v_{\text{ref}} - v_h /v_{\text{ref}} \times 100$) at point B in the infinite plate with a circular hole. | 21 |
| Table 2.4. Relative errors in the horizontal displacement ($ u_{\text{ref}} - u_h /u_{\text{ref}} \times 100$) at point A in Cook's skew beam problem. | 21 |
| Table 2.5. Relative errors in the vertical displacement ($ v_{\text{ref}} - v_h /v_{\text{ref}} \times 100$) at point A in the ring problem. .. | 22 |

List of Figures

| | |
|--|----|
| Fig. 2.1. Strain fields of 3-node triangular elements: (a) The strain fields of standard 3-node triangular elements. (b) The strain fields of the edge-based S-FEM within smoothing domains. Based on the edge (red line), the smoothing domains between two adjacent elements are formed. (c) The strain field within a 3-node triangular element through SSE method. The smoothed strains are assigned to the Gauss integration points. | 4 |
| Fig. 2.2. Procedure of the SSE method in a 4-node quadrilateral element: (a) Four sub-triangles of a 4-node quadrilateral element. (b) The smoothed strains $\hat{\boldsymbol{\epsilon}}^{(i)}$. The smoothed strains are obtained through smoothing of neighboring strain fields based on the edge. (c) The smoothed strains $\bar{\boldsymbol{\epsilon}}_i$ are assigned to the Gauss integration points of the quadrilateral element. | 6 |
| Fig. 2.3. Triangulation of a polygonal element and all integration points in sub-triangles. | 7 |
| Fig. 2.4. (a) A polygonal element and its sub-triangles. (b) Natural coordinate system for a sub-triangle. | 8 |
| Fig. 2.5. A mesh of polygonal elements: (a) Target element m and its neighboring elements. (b) The strains of the k th sub-triangle of the target element and its adjacent sub-triangle in the neighboring element. | 9 |
| Fig. 2.6. Sub-triangles and nodes of an element. | 9 |
| Fig. 2.7. Strain smoothing procedure in the strain-smoothed polygonal elements: (a) Triangulation of the polygonal element. The smoothed strain $\hat{\boldsymbol{\epsilon}}^{(k)}$ corresponding to the k th sub-triangle. (b) Quadrangulation of the polygonal element. The smoothed strain $\bar{\boldsymbol{\epsilon}}_k$ assigned to the center point of the k th sub-quadrilateral. (c) Calculation of the nodal strains $\bar{\boldsymbol{\epsilon}}_{n1}^{(k)}$ and $\bar{\boldsymbol{\epsilon}}_{n2}^{(k)}$ for the k th sub-triangle. | 11 |
| Fig. 2.8. Position vector of an arbitrary point \mathbf{x}_k in the triangular domain. | 12 |
| Fig. 2.9. Signed area of a sub-triangle when (a) $A_k^{(m)} > 0$, (b) $A_k^{(m)} = 0$, and (c) $A_k^{(m)} < 0$ | 13 |
| Fig. 2.10. Different node numbering sequences for a polygonal element. | 14 |
| Fig. 2.11. Polygonal meshes used for the zero-energy mode test. | 16 |
| Fig. 2.12. A polygonal mesh used for the patch tests. | 16 |
| Fig. 2.13. Infinite plate with a circular hole ($E = 3 \times 10^7$ and $\nu = 0.3$). Only shaded domain is meshed due to symmetry. | 23 |
| Fig. 2.14. Polygonal meshes used for the infinite plate with a circular hole. | 23 |
| Fig. 2.15. Convergence curves for the infinite plate with a circular hole. The bold line represents the optimal convergence rate. | 24 |
| Fig. 2.16. Stress distributions (σ_{xy}) for the infinite plate with a circular hole. Only 2.5×2.5 area around the hole is plotted. The reference stress distribution is obtained using an 8,192 element mesh of 9-node quadrilateral elements. | 25 |
| Fig. 2.17. Cook's skew beam ($E = 3 \times 10^7$ and $\nu = 0.3$). | 26 |
| Fig. 2.18. Polygonal meshes used for Cook's skew beam. | 26 |
| Fig. 2.19. Convergence curves for Cook's skew beam. The bold line represents the optimal convergence rate. . | 27 |
| Fig. 2.20. Normalized horizontal displacements (u_h/u_{ref}) at point A in Cook's skew beam. | 27 |
| Fig. 2.21. Computational efficiency curves for Cook's skew beam. The computation times are measured in seconds. | 28 |
| Fig. 2.22. Mesh obtained by triangulation of polygons ($N = 4$): (a) Polygonal mesh (92 DOFs). (b) Triangular mesh (136 DOFs). | 28 |

| | |
|---|----|
| Fig. 2.23. Dam problem ($E = 3 \times 10^{10}$ and $\nu = 0.2$). | 29 |
| Fig. 2.24. Polygonal meshes used for the dam problem. | 29 |
| Fig. 2.25. Convergence curves for the dam problem. The bold line represents the optimal convergence rate. .. | 30 |
| Fig. 2.26. Polygonal meshes constructed using the paving and cutting algorithm for the dam problem. | 31 |
| Fig. 2.27. Convergence curves for the dam problem when the meshes with the paving and cutting algorithm are utilized. The bold line represents the optimal convergence rate. | 31 |
| Fig. 2.28. Ring problem ($E = 3 \times 10^3$ and $\nu = 0.3$). Only shaded domain is considered for analysis owing to symmetry. | 32 |
| Fig. 2.29. Polygonal meshes constructed using the paving and cutting algorithm for the ring problem. | 32 |
| Fig. 2.30. Convergence curves for the ring problem. The bold line represents the optimal convergence rate. ... | 33 |
| Fig. 2.31. von Mises stress distributions for the ring problem. The reference stress distribution is obtained using a 64×64 mesh of 9-node quadrilateral elements. | 34 |
| Fig. 2.32. Normalized vertical displacements (v_h/v_{ref}) at point A in the ring problem. | 35 |
| Fig. 3.1. Hydrostatic pressure and volume change. | 37 |
| Fig. 3.2. Integration points for the deviatoric and volumetric term in the 4-node quadrilateral finite element. ... | 39 |
| Fig. 3.3. The 4-node strain-smoothed element: (a) smoothed strain through the edges, (b) a deviatoric strain field, (c) a constant volumetric strain field. | 40 |
| Fig. 3.4. The assumed volumetric strain in the strain-smoothed polygonal finite element. | 41 |
| Fig. 3.5. The linear strain field within a 3-node triangular element through SSE method. | 43 |
| Fig. 3.6. A node and its neighboring integration points in a triangular mesh. | 43 |
| Fig. 3.7. The nodal smoothed volumetric strain obtained from the neighboring smoothed strains. | 44 |
| Fig. 3.8. Nodal smoothed volumetric strains and a volumetric strain field within an element. | 45 |
| Fig. 3.9. (a) Smoothing domains for the node-based smoothed finite element. (b) A strain field within an element for the strain-smoothed element. | 46 |
| Fig. 3.10. A 2D triangular finite mesh used for the patch test. | 47 |
| Fig. 3.11. The uniform stress conditions for the patch test. | 48 |
| Fig. 3.12. (a) The square block problem ($E = 3 \times 10^7$ and $\nu = 0.3, 0.49, 0.499$ and 0.4999). (b) A regular mesh and (c) a distorted mesh at $N = 4$ used for the square block problem. | 50 |
| Fig. 3.13. Distorted meshes used for the square block problem. | 50 |
| Fig. 3.14. Convergence curves for the square block problem with regular meshes. The bold line represents the optimal convergence rate. | 51 |
| Fig. 3.15. Convergence curves for the square block problem with distorted meshes. The bold line represents the optimal convergence rate. | 51 |
| Fig. 3.16. (a) Infinite plate with a circular hole ($E = 3 \times 10^7$ and $\nu = 0.3, 0.49, 0.499$ and 0.4999). (b) A mesh at $N = 8$ used for the problem. | 53 |
| Fig. 3.17. Convergence curves for the problem of infinite plate with a circular hole. The bold line represents the optimal convergence rate. | 53 |
| Fig. 3.18 (a) The Cook's skew beam problem ($E = 3 \times 10^7$ and $\nu = 0.3, 0.49, 0.499$ and 0.4999). (b) A regular mesh and (c) a distorted mesh at $N = 4$ used for the cook's beam problem. | 55 |
| Fig. 3.19. Examples of distorted meshes used for the Cook's skew beam problem. | 56 |
| Fig. 3.20. Convergence curves for the Cook's skew beam problem with regular meshes. The bold line represents | 56 |

| | |
|---|----|
| the optimal convergence rate. | 56 |
| Fig. 3.21. Convergence curves for the Cook's skew beam problem with distorted meshes. The bold line represents the optimal convergence rate. | 57 |
| Fig. 3.22. (a) Dam problem ($E = 3 \times 10^{10}$ and $\nu = 0.3, 0.49, 0.499$ and 0.4999). (b) A mesh at $N = 4$ used for the dam problem. | 58 |
| Fig. 3.23. Convergence curves for the dam problem. The bold line represents the optimal convergence rate. | 59 |

Chapter 1. Introduction

The finite element method (FEM) has been widely used to analyze problems in various scientific and engineering fields [1-3]. The accuracy of finite element solutions relies upon the quality of the meshes used. However, because the geometries used in engineering practice are very complex, considerable effort is required to create well-shaped meshes. Conventional triangular and quadrilateral finite elements have usually been preferred owing to their efficiency and simplicity [4].

Recently, polygonal finite elements have been investigated as they can provide a high level of flexibility in mesh generation, transition, and refinement [4-20]; simpler meshing algorithms are possible, such as conformal decomposition [5-8] and Voronoi tessellations [9,10]. They can effectively solve various problems such as contact problems on non-conformal meshes [6,11], crack propagation problems with minimum remeshing [8,12], and the modeling of polycrystalline materials [13]. Further research is required to develop polygonal finite elements that provide more accurate and reliable solutions.

Polygonal finite elements typically adopt barycentric coordinates to construct shape functions, such as Wachspress coordinates [14] and mean value coordinates [15]. In these coordinates, the shape functions are constructed in the form of rational functions using the sub-areas or interior angles of an element. Then, it is difficult to accurately calculate the stiffness matrix through numerical integration. Numerous studies pertaining to the numerical integration of polygonal elements have been conducted [4,16-20]. Instead, piecewise linear shape functions can be introduced such that numerical integration can be performed easily for each sub-triangle of the polygonal element [4,20].

Various strain smoothing techniques have been successfully developed for the FEM [21-33]. A distinct feature is that no additional degrees of freedom are required for the solution improvement. In well-known smoothed finite element methods (S-FEMs), special smoothing domains are constructed based on a cell, node, edge, or face [22-30]. In these methods, the neighboring strains for performing the smoothing technique are determined according to the smoothing domains, and constant strain fields are constructed in the domains.

The recently proposed strain-smoothed element (SSE) method provides further improved solutions without requiring the construction of specific smoothing domains, unlike existing strain smoothing techniques. The linear strain field within an element is formed from the constant strain fields of neighboring elements obtained from simple strain smoothing. The SSE method has been successfully applied to 3-node triangular and 4-node quadrilateral 2D solid elements, and a 3-node MITC3+ shell element [31-33]. Recently, a variational framework for the SSE method has been studied [34].

In this study, the SSE method is applied to polygonal finite elements to generate strain-smoothed polygonal elements. Piecewise linear shape functions are employed and strain smoothing is performed via the triangulation of polygonal elements. The polygonal elements have a smoothed strain field within the element, which is constructed by assigning smoothed strain values to the vertices of the sub-triangles. The proposed elements show further improved convergence behaviors compared with the existing polygonal elements in various numerical examples.

In addition, volumetric locking is a phenomenon that occurs in most elements depending on the material properties. As the Poisson's ratio approaches 0.5, the bulk modulus becomes significantly larger, resulting in a stiffening of the elements. To address this issue, numerous studies have been conducted. For example, research has explored methods to soften the elements through reduced integration or has introduced additional degrees of freedom related to pressure to resolve the problem [40-43]. Reduced integration allowed for an easier way to soften elements without increasing degrees of freedom, but this led to the occurrence of spurious zero-energy modes (or hourglass modes). Later, a method called 'selective reduced integration' was proposed, which assumed strain related to volumetric changes and performed reduced integration only for the volumetric terms. This approach can be easily applied to many elements.

Smoothing elements have significantly improved the performance of elements but still suffer from the same issue of volumetric locking. To alleviate the locking, the node-based smoothing can be applied, which has the feature of being overly-soft compared to other elements, thus avoiding volumetric locking [44]. However, there is a slight issue with the performance of the element. For the 4-node rectangular element with the SSE method, the assuming constant smoothed volumetric strain field is applied to address volumetric locking [33]. Like the selective reduced integration, assuming constant volumetric strain can be applied to various elements, including smoothed elements. However, it cannot be directly applied to 3-node triangular elements, where the strain field of the element is already constant.

In this study, the new volumetric strain is defined using the smoothed strains assigned to the integration points through strain-smoothed element method. Similar to the application of selective reduced integration, the volumetric and deviatoric strains are assumed using the smoothed strains. The deviatoric terms are integrated within the element similar to the process in SSE, and new volumetric strain is obtained by performing node-wise smoothing process using the smoothed strains from the integration points near the node. The proposed element, the strain-smoothed 3-node triangular finite element with nodal volumetric smoothed strains, provides improved convergence performance in situations far from volumetric locking, and the element exhibits convergence behavior with alleviated volumetric locking, even in situations where volumetric locking occurs in various numerical examples.

Chapter 2. Strain-smoothed polygonal finite elements

In this chapter, the SSE method is applied to polygonal finite elements and improved performance of the strain-smoothed polygonal finite elements is demonstrated through numerical examples. For strain smoothing between neighboring elements and numerical integration of polygonal elements, polygonal elements are divided into several sub-triangles based on the center point, and the piecewise linear shape functions are utilized. The proposed elements are constructed of piecewise linear strain field within the elements through Gauss integration points in the sub-triangles.

we briefly introduce the strain-smoothed element method and polygonal elements, and present the formulation of the strain-smoothed polygonal finite elements, including the interpolations of geometry and displacement, strain smoothing, strain-displacement relation, and stiffness matrix.

2.1 Strain-smoothed element method for 2D solid elements

The strain-smoothed element (SSE) method has been applied to 3-node and 4-node elements for 2D solid elements. To apply the SSE method, neighboring strains based on the all edges of an element are used. For the standard 3-node triangular 2D solid element, the geometry is described by

$$\mathbf{x} = h_1 \mathbf{x}_1 + h_2 \mathbf{x}_2 + h_3 \mathbf{x}_3 \quad \text{with} \quad \mathbf{x}_i = [x_i \quad y_i]^T, \quad (2.1)$$

where \mathbf{x}_i is the position vector of node i in the global Cartesian coordinate system, and $h_i(r, s)$ correspond to the shape functions of the standard isoparametric procedure given by

$$h_1 = r, \quad h_2 = s, \quad h_3 = 1 - r - s. \quad (2.2)$$

The displacement of the standard 3-node triangular 2D solid element is expressed by

$$\mathbf{u} = h_1 \mathbf{u}_1 + h_2 \mathbf{u}_2 + h_3 \mathbf{u}_3 \quad \text{with} \quad \mathbf{u}_k = [u_k \quad v_k]^T, \quad (2.3)$$

where \mathbf{u}_i is the displacement vector of node i in the global Cartesian coordinate system.

Through the standard isoparametric finite element procedure [1], the strain field within the 3-node triangular element m is defined as

$$\boldsymbol{\varepsilon}^{(m)} = [\varepsilon_{11} \quad \varepsilon_{22} \quad 2\varepsilon_{12}]^T = \mathbf{B}^{(m)} \mathbf{u}^{(m)} \quad \text{with} \quad \mathbf{B}^{(m)} = [\mathbf{B}_1 \quad \mathbf{B}_2 \quad \mathbf{B}_3], \quad \mathbf{u}^{(m)} = [\mathbf{u}_1 \quad \mathbf{u}_2 \quad \mathbf{u}_3]^T, \quad (2.4)$$

in which $\mathbf{B}^{(m)}$ is the strain-displacement matrix of the element m , \mathbf{B}_i is the strain-displacement matrix corresponding to node i , and $\mathbf{u}^{(m)}$ is the nodal displacement vector of the element m .

In the standard 3-node triangular element, a constant strain field is constructed within an element as shown in **Fig. 2.1(a)**. In the edge-based S-FEM, two neighboring strain fields based on the edge are used for smoothing process. The smoothed strain based on the edge is given by

$$\hat{\boldsymbol{\varepsilon}}^{(i)} = \frac{1}{A^{(e)} + A^{(i)}} (A^{(e)} \boldsymbol{\varepsilon}^{(e)} + A^{(i)} \boldsymbol{\varepsilon}^{(i)}) \quad (2.5)$$

where $A^{(e)}$ and $A^{(i)}$ are the areas of the target element e and neighboring element i , and $\boldsymbol{\varepsilon}^{(e)}$ and $\boldsymbol{\varepsilon}^{(i)}$ are the strains of the target element e and neighboring element i . In the edge-based S-FEM, the smoothed strains are assigned into smoothing domains between two adjacent elements, as shown in **Fig. 2.1(b)**. The smoothing domains are obtained by dividing each element based on the center point of the element [22].

In the SSE method, the strains of all neighboring elements are used for constructing strain fields within an element [31]. In a 3-node triangular element, there are three Gauss integration points, as shown in **Fig. 2.1(c)**. In order to construct a strain field within the element, smoothed strain values are assigned to Gauss integration points using strains obtained based on the edges using the following equations, as shown in **Fig. 2.1(c)**

$$\bar{\boldsymbol{\varepsilon}}_1 = \frac{1}{2} (\hat{\boldsymbol{\varepsilon}}^{(1)} + \hat{\boldsymbol{\varepsilon}}^{(3)}), \quad \bar{\boldsymbol{\varepsilon}}_2 = \frac{1}{2} (\hat{\boldsymbol{\varepsilon}}^{(1)} + \hat{\boldsymbol{\varepsilon}}^{(2)}), \quad \bar{\boldsymbol{\varepsilon}}_3 = \frac{1}{2} (\hat{\boldsymbol{\varepsilon}}^{(2)} + \hat{\boldsymbol{\varepsilon}}^{(3)}). \quad (2.6)$$

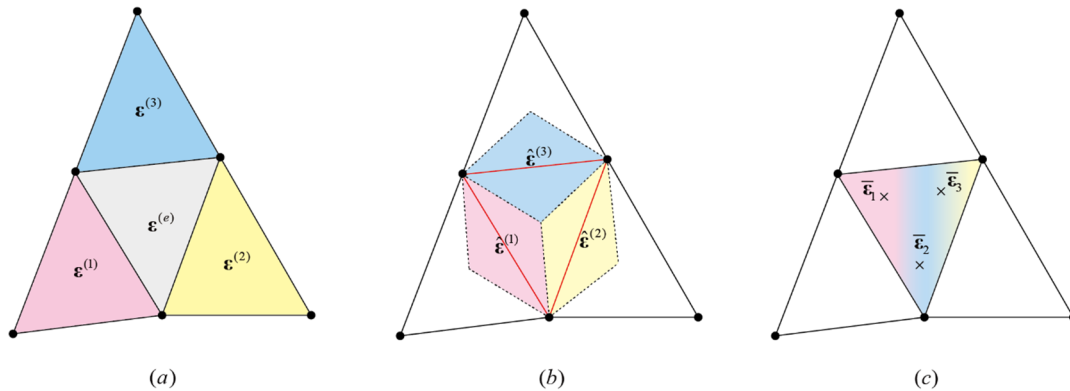


Fig. 2.1. Strain fields of 3-node triangular elements: (a) The strain fields of standard 3-node triangular elements. (b) The strain fields of the edge-based S-FEM within smoothing domains. Based on the edge (red line), the smoothing domains between two adjacent elements are formed. (c) The strain field within a 3-node triangular element through SSE method. The smoothed strains are assigned to the Gauss integration points.

For the standard 4-node quadrilateral 2D solid element, the element is divided into four sub-triangles based on the center point to perform the smoothing process [33]. The position vector of the center point, \mathbf{x}_c , is defined using the nodal position vectors \mathbf{x}_i ($i = 1, 2, 3, 4$) as follows:

$$\mathbf{x}_c = \frac{1}{4} \sum_{i=1}^4 \mathbf{x}_i \quad \text{with} \quad \mathbf{x}_i = [x_i \quad y_i]^T. \quad (2.7)$$

The geometry of the sub-triangle T1 of the 4-node element shown in **Fig. 2.2(a)** can be represented by

$$\mathbf{x} = h_1 \mathbf{x}_1 + h_2 \mathbf{x}_2 + h_3 \mathbf{x}_c, \quad (2.8)$$

where $h_i(r, s)$ correspond to the shape functions of the standard isoparametric procedure for the 3-node triangular domain,

$$h_1 = r, \quad h_2 = s, \quad h_3 = 1 - r - s. \quad (2.9)$$

The geometries of other sub-triangles are also defined by own natural coordinates.

For the piecewise linear shape functions in the 4-node element, piecewise constant strain fields are constructed based on the sub-triangles. The strain field in the k th sub-triangle of the element m is defined as

$${}^k \boldsymbol{\varepsilon}^{(m)} = {}^k \mathbf{B}^{(m)} \mathbf{u}^{(m)} \quad \text{with} \quad {}^k \mathbf{B}^{(m)} = [{}^k \mathbf{B}_1 \quad {}^k \mathbf{B}_2 \quad {}^k \mathbf{B}_3 \quad {}^k \mathbf{B}_4], \quad \mathbf{u}^{(m)} = [\mathbf{u}_1 \quad \mathbf{u}_2 \quad \mathbf{u}_3 \quad \mathbf{u}_4]^T, \quad (2.10)$$

in which ${}^k \mathbf{B}^{(m)}$ is the strain-displacement matrix of k th sub-triangle of the element m , ${}^k \mathbf{B}_i$ is the strain-displacement matrix corresponding to node i , and $\mathbf{u}^{(m)}$ is the nodal displacement vector of the element m .

Similar to the process in the triangular element, the smoothed strain based on the edge (as shown in **Fig. 2.2(b)**) is given by

$$\hat{\boldsymbol{\varepsilon}}^{(k)} = \frac{1}{A_k^{(m)} + A^{(k)}} (A_k^{(m)} {}^k \boldsymbol{\varepsilon}^{(m)} + A^{(k)} \boldsymbol{\varepsilon}^{(k)}) \quad (2.11)$$

where ${}^k \boldsymbol{\varepsilon}^{(m)}$ and $A_k^{(m)}$ are the strain and area of the k th sub-triangle of the target element m , and $\boldsymbol{\varepsilon}^{(k)}$ and $A^{(k)}$ are the strain and area of its neighboring sub-triangle, respectively.

As shown in **Fig. 2.2(c)**, smoothed strains $\bar{\boldsymbol{\varepsilon}}_i$ are assigned to Gauss integration points using smoothed strains

$\hat{\boldsymbol{\varepsilon}}^{(i)}$ using the following equations,

$$\bar{\boldsymbol{\varepsilon}}_k = \frac{1}{A_{k-1}^{(m)} + A_k^{(m)}} (A_{k-1}^{(m)} \hat{\boldsymbol{\varepsilon}}^{(k-1)} + A_k^{(m)} \hat{\boldsymbol{\varepsilon}}^{(k)}) \quad \text{with} \quad k = 1, 2, 3, 4, \quad (2.12)$$

in which $\hat{\boldsymbol{\varepsilon}}^{(0)} = \hat{\boldsymbol{\varepsilon}}^{(4)}$ and $A_0^{(m)} = A_4^{(m)}$.

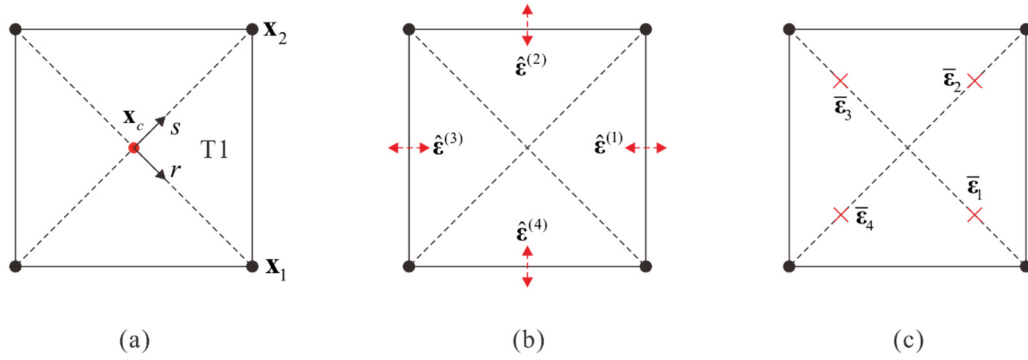


Fig. 2.2. Procedure of the SSE method in a 4-node quadrilateral element: (a) Four sub-triangles of a 4-node quadrilateral element. (b) The smoothed strains $\hat{\boldsymbol{\varepsilon}}^{(i)}$. The smoothed strains are obtained through smoothing of neighboring strain fields based on the edge. (c) The smoothed strains $\bar{\boldsymbol{\varepsilon}}_i$ are assigned to the Gauss integration points of the quadrilateral element.

2.2 Formulation of the strain-smoothed polygonal finite element

2.2.1 Integration of polygonal elements

The polygonal elements can have five or more edges; thus, it is very difficult to extend the Gauss quadrature rules from the triangular and quadrilateral elements to polygonal elements. In order to apply the standard Gauss quadrature rules, methods for dividing polygons have been proposed [4,19]. As a representative method among these, a polygonal element is divided into several sub-triangles based on the center point of the polygon, and integration is performed using standard Gauss integration points for a triangular element as shown in **Fig. 2.3**.

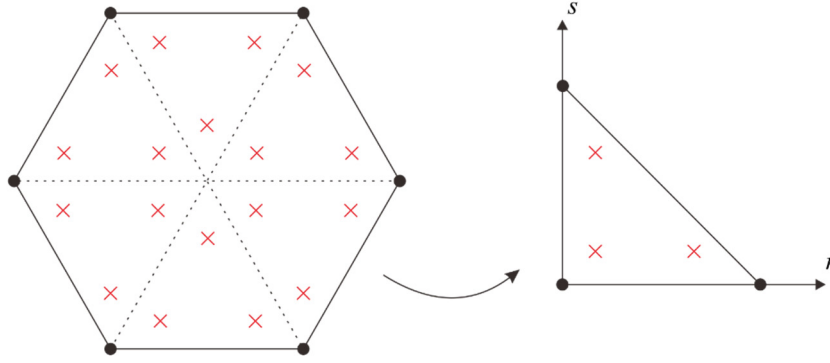


Fig. 2.3. Triangulation of a polygonal element and all integration points in sub-triangles.

2.2.2 Geometry and displacement interpolations

An n -sided polygonal element can be segmented into n sub-triangles based on its nodes and center point, as shown in **Fig. 2.4(a)**. The position vector of the center point, \mathbf{x}_c , is defined using the nodal position vectors \mathbf{x}_i ($i = 1, 2, \dots, n$) as follows:

$$\mathbf{x}_c = \frac{1}{n} \sum_{i=1}^n \mathbf{x}_i \quad \text{with} \quad \mathbf{x}_i = [x_i \quad y_i]^T. \quad (2.13)$$

The geometry of the k th sub-triangle of the polygonal element shown in **Fig. 2.4** can be represented by

$$\mathbf{x} = h_1 \mathbf{x}_{k-1} + h_2 \mathbf{x}_k + h_3 \mathbf{x}_c, \quad (2.14)$$

where \mathbf{x}_{k-1} and \mathbf{x}_k refer to the set of position vectors of two neighboring nodes with $\mathbf{x}_0 = \mathbf{x}_n$; $h_i(r, s)$ correspond to the shape functions of the standard isoparametric procedure for the 3-node triangular domain,

$$h_1 = r, \quad h_2 = s, \quad h_3 = 1 - r - s. \quad (2.15)$$

Based on Eq. (2.14), the displacement interpolation of the k th sub-triangle of the n -sided polygonal element can be expressed as

$$\mathbf{u} = h_1 \mathbf{u}_{k-1} + h_2 \mathbf{u}_k + h_3 \mathbf{u}_c \quad \text{with} \quad \mathbf{u}_k = [u_k \quad v_k]^T, \quad (2.16)$$

$$\mathbf{u}_c = \frac{1}{n} \sum_{i=1}^n \mathbf{u}_i, \quad (2.17)$$

where \mathbf{u}_k is the displacement vector of node k , and \mathbf{u}_c is the displacement vector of the center point of the polygonal element.

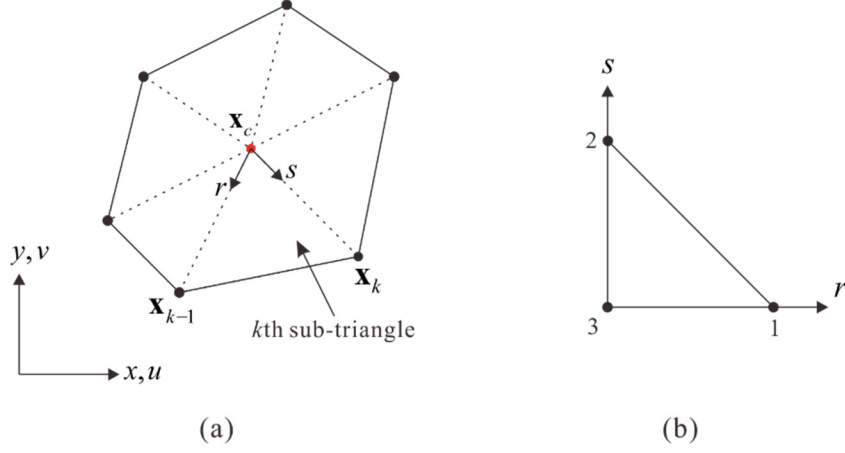


Fig. 2.4. (a) A polygonal element and its sub-triangles. (b) Natural coordinate system for a sub-triangle.

2.2.3 Strain smoothing

We consider the n -sided polygonal element m in a finite element mesh, as shown in **Fig. 2.5**. By adopting the standard isoparametric finite element procedure [1], the strain field within the k th sub-triangle of the target element m is defined as

$${}^k \boldsymbol{\varepsilon}^{(m)} = [\varepsilon_{11} \quad \varepsilon_{22} \quad 2\varepsilon_{12}]^T = {}^k \mathbf{B}^{(m)} \mathbf{u}^{(m)} \quad \text{with } k = 1, 2, \dots, n, \quad (2.18)$$

$${}^k \mathbf{B}^{(m)} = [{}^k \mathbf{B}_1 \quad {}^k \mathbf{B}_2 \quad \dots \quad {}^k \mathbf{B}_n], \quad (2.19)$$

$${}^k \mathbf{B}_i = \begin{bmatrix} \delta_{ik} h_{1,x} + \delta_{i(k+1)} h_{2,x} + \frac{1}{n} h_{3,x} & 0 & \delta_{ik} h_{1,y} + \delta_{i(k+1)} h_{2,y} + \frac{1}{n} h_{3,y} \\ 0 & \delta_{ik} h_{1,y} + \delta_{i(k+1)} h_{2,y} + \frac{1}{n} h_{3,y} & \delta_{ik} h_{1,x} + \delta_{i(k+1)} h_{2,x} + \frac{1}{n} h_{3,x} \end{bmatrix}^T, \quad (2.20)$$

$$\mathbf{u}^{(m)} = [\mathbf{u}_1 \quad \mathbf{u}_2 \quad \dots \quad \mathbf{u}_n]^T \quad \text{with } \mathbf{u}_i = [u_i \quad v_i]^T, \quad (2.21)$$

where ${}^k \mathbf{B}^{(m)}$ is the strain-displacement matrix of the k th sub-triangle, ${}^k \mathbf{B}_i$ is the strain-displacement matrix corresponding to node i , δ_{ik} is the Kronecker delta, and $\mathbf{u}^{(m)}$ is the nodal displacement vector of the target element m , see **Fig. 2.5(b)** and **Fig. 2.6**.

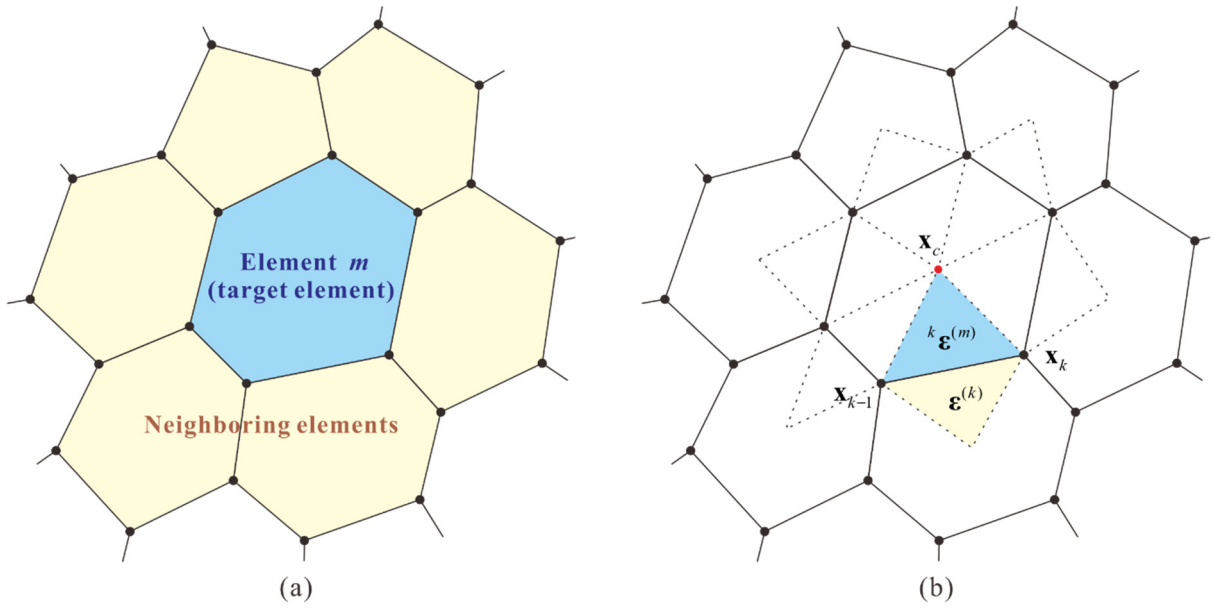


Fig. 2.5. A mesh of polygonal elements: (a) Target element m and its neighboring elements. (b) The strains of the k th sub-triangle of the target element and its adjacent sub-triangle in the neighboring element.

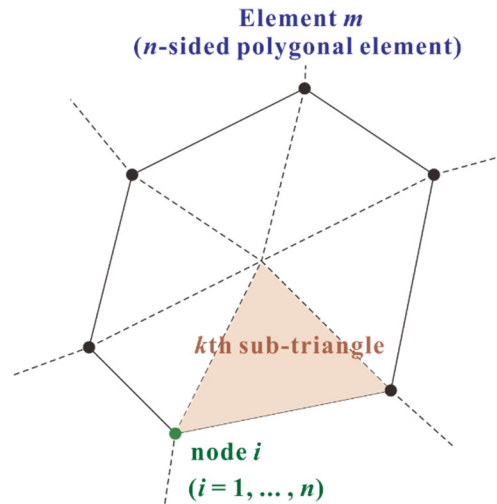


Fig. 2.6. Sub-triangles and nodes of an element.

The n -sided polygonal element can have a maximum of n adjacent elements through its n element edges, as shown in Fig. 2.5. The smoothed strain between the k th sub-triangle of the target element m and its adjacent sub-triangle of the neighboring element is calculated as follows:

$$\hat{\boldsymbol{\epsilon}}^{(k)} = \frac{1}{A_k^{(m)} + A^{(k)}} (A_k^{(m)} \boldsymbol{\epsilon}^{(m)} + A^{(k)} \boldsymbol{\epsilon}^{(k)}) \quad \text{with } k = 1, 2, \dots, n, \quad (2.22)$$

where ${}^k \boldsymbol{\varepsilon}^{(m)}$ and $A_k^{(m)}$ are the (constant) strain and area of the k th sub-triangle of the target element m , respectively; $\boldsymbol{\varepsilon}^{(k)}$ and $A^{(k)}$ are the strain and area of its neighboring sub-triangle, respectively. If no element is adjacent to the k th sub-triangle, then $\hat{\boldsymbol{\varepsilon}}^{(k)} = {}^k \boldsymbol{\varepsilon}^{(m)}$ is adopted [31].

It is noteworthy that $\hat{\boldsymbol{\varepsilon}}^{(k)}$ in Eq. (2.22) is the smoothed strain representing the k th sub-triangle as shown in **Fig. 2.7(a)**. Additionally, we can partition the polygonal element into n sub-quadrilaterals by combining the halves of two neighboring sub-triangles as shown in **Fig. 2.7(b)**. Subsequently, the smoothed strain corresponding to the k th sub-quadrilateral of the target element m is defined as

$$\bar{\boldsymbol{\varepsilon}}_k = \frac{1}{A_k^{(m)} + A_{k+1}^{(m)}} (A_k^{(m)} \hat{\boldsymbol{\varepsilon}}^{(k)} + A_{k+1}^{(m)} \hat{\boldsymbol{\varepsilon}}^{(k+1)}) \quad \text{with } k = 1, 2, \dots, n, \quad (2.23)$$

in which $\hat{\boldsymbol{\varepsilon}}^{(n+1)} = \hat{\boldsymbol{\varepsilon}}^{(1)}$ and $A_{n+1}^{(m)} = A_1^{(m)}$. The smoothed strain $\bar{\boldsymbol{\varepsilon}}_k$ is assigned to the center point of the k th sub-quadrilateral.

The smoothed strains for all the sub-quadrilaterals in Eq. (2.23) are utilized to calculate the strain at the center point of the polygonal element, as shown in **Fig. 2.7(b)**,

$$\bar{\boldsymbol{\varepsilon}}_c = \frac{\sum_{k=1}^n A_k^{(m)} \bar{\boldsymbol{\varepsilon}}_k}{\sum_{k=1}^n A_k^{(m)}}. \quad (2.24)$$

Subsequently, we calculate the nodal strains for the sub-triangles by assigning the strains in Eq. (2.23) to the center point of each sub-quadrilateral, and the strain in Eq. (2.24) to the center point of the polygonal element, as shown in **Fig. 2.7(c)**. For nodal strains $\bar{\boldsymbol{\varepsilon}}_{n1}^{(k)}$ and $\bar{\boldsymbol{\varepsilon}}_{n2}^{(k)}$ in the k th sub-triangle, the components of the nodal strains,

$\bar{\boldsymbol{\varepsilon}}_{n1}^{(k)}$ and $\bar{\boldsymbol{\varepsilon}}_{n2}^{(k)}$, are obtained as follows:

$$\begin{bmatrix} \bar{\boldsymbol{\varepsilon}}_{n1}^{(k)} \\ \bar{\boldsymbol{\varepsilon}}_{n2}^{(k)} \end{bmatrix} = \begin{bmatrix} r_1 & s_1 \\ r_2 & s_2 \end{bmatrix}^{-1} \begin{bmatrix} \bar{\boldsymbol{\varepsilon}}_{k-1} - \bar{\boldsymbol{\varepsilon}}_c (1 - r_1 - s_1) \\ \bar{\boldsymbol{\varepsilon}}_k - \bar{\boldsymbol{\varepsilon}}_c (1 - r_2 - s_2) \end{bmatrix}, \quad (2.25)$$

where (r_1, s_1) and (r_2, s_2) are the natural coordinates of the allocated points of the smoothed strains $\bar{\boldsymbol{\varepsilon}}_{k-1}$ and $\bar{\boldsymbol{\varepsilon}}_k$, respectively (see **Fig. 2.7(c)**).

Using the nodal strains and the strain at the center point in Eq. (2.24), the smoothed strain field within the element is determined via the linear interpolation for each sub-triangle. Similar to Eq. (2.2), the smoothed strain field within the k th sub-triangle of the element m is expressed as

$${}^k\bar{\boldsymbol{\epsilon}}^{(m)} = h_1 \bar{\boldsymbol{\epsilon}}_{n1}^{(k)} + h_2 \bar{\boldsymbol{\epsilon}}_{n2}^{(k)} + h_3 \bar{\boldsymbol{\epsilon}}_c. \quad (2.26)$$

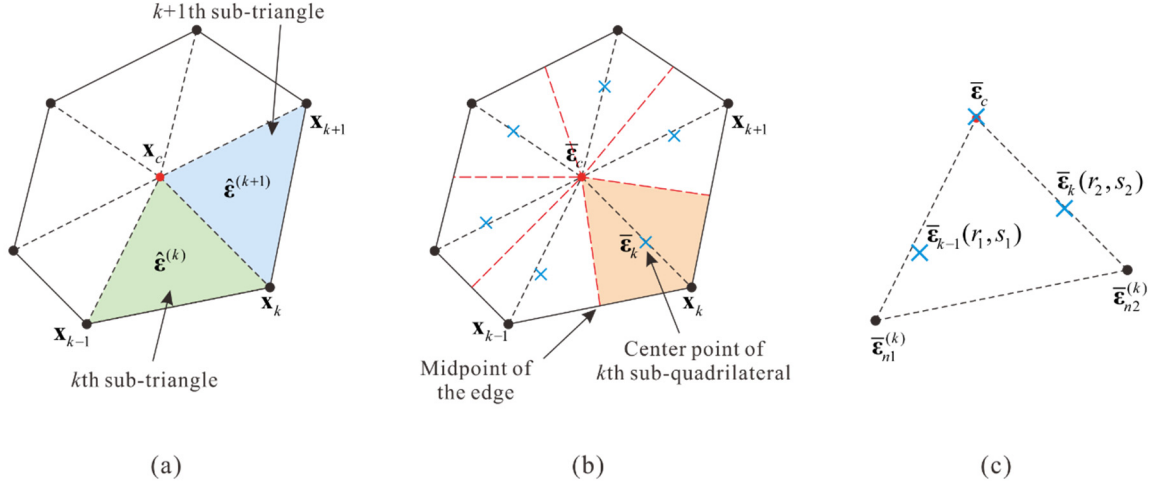


Fig. 2.7. Strain smoothing procedure in the strain-smoothed polygonal elements: (a) Triangulation of the polygonal element. The smoothed strain $\hat{\boldsymbol{\epsilon}}^{(k)}$ corresponding to the k th sub-triangle. (b) Quadrangulation of the polygonal element. The smoothed strain $\bar{\boldsymbol{\epsilon}}_k$ assigned to the center point of the k th sub-quadrilateral. (c) Calculation of the nodal strains $\bar{\boldsymbol{\epsilon}}_{n1}^{(k)}$ and $\bar{\boldsymbol{\epsilon}}_{n2}^{(k)}$ for the k th sub-triangle.

The process for obtaining the natural coordinates (r_i, s_i) in Eq. (2.25) proceeds like linear extrapolation. The position vector of a point \mathbf{x}_k in the triangular domain shown in **Fig. 2.8** can be expressed using the shape functions of the standard isoparametric procedure as follows:

$$\mathbf{x}_k = r_k \mathbf{x}_1 + s_k \mathbf{x}_2 + (1 - r_k - s_k) \mathbf{x}_3, \quad (2.27)$$

where \mathbf{x}_1 , \mathbf{x}_2 , and \mathbf{x}_3 are the position vectors of the vertices of the triangular domain; r_k and s_k are the natural coordinates of \mathbf{x}_k to be determined.

The natural coordinates r_k and s_k are unknown values, and the positions of vertices $\mathbf{x}_i(x_i, y_i)$ and point \mathbf{x}_k are specified. Eq. (2.27) can be expressed using the following matrix equation:

$$\begin{bmatrix} x_1 - x_3 & x_2 - x_3 \\ y_1 - y_3 & y_2 - y_3 \end{bmatrix} \begin{bmatrix} r_k \\ s_k \end{bmatrix} = \begin{bmatrix} x_k - x_3 \\ y_k - y_3 \end{bmatrix}, \quad (2.28)$$

where (x_i, y_i) is the coordinates of \mathbf{x}_i in the Cartesian coordinate system.

Finally, the natural coordinates r_k and s_k are calculated as follows:

$$\begin{bmatrix} r_k \\ s_k \end{bmatrix} = \begin{bmatrix} x_1 - x_3 & x_2 - x_3 \\ y_1 - y_3 & y_2 - y_3 \end{bmatrix}^{-1} \begin{bmatrix} x_k - x_3 \\ y_k - y_3 \end{bmatrix}. \quad (2.29)$$

In general, natural coordinates in the triangular domain are defined between 0 and 1; however, if the position \mathbf{x}_k is located outside the domain, the natural coordinates r_k and s_k can be negative values. Using the nodal strains and the strain at the center point in Eq. (2.24), the smoothed strain field within the element is determined via the linear interpolation for each sub-triangle.

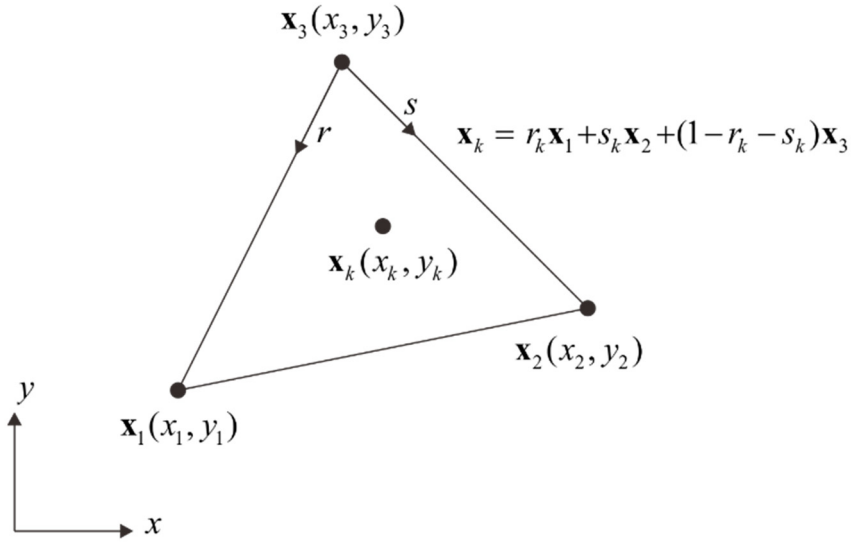


Fig. 2.8. Position vector of an arbitrary point \mathbf{x}_k in the triangular domain.

2.2.4 Strain-displacement relation and stiffness matrix

Let us consider the n -sided polygonal finite element m with n neighboring elements through its edges, as shown in Fig. 2.5. In the k th sub-triangle of the element m , the relation between the smoothed strain field and the nodal displacement vector is given by

$${}^k \bar{\boldsymbol{\epsilon}}^{(m)} = {}^k \bar{\mathbf{B}}^{(m)} \bar{\mathbf{u}}^{(m)} \quad (2.30)$$

with

$${}^k \bar{\mathbf{B}}^{(m)} = \left[\bar{\mathbf{B}}_1 \quad \bar{\mathbf{B}}_2 \quad \cdots \quad \bar{\mathbf{B}}_l \right], \quad (2.31)$$

where ${}^k \bar{\boldsymbol{\epsilon}}^{(m)}$ is the smoothed strain field of the target element m , ${}^k \bar{\mathbf{B}}^{(m)}$ is the strain-displacement matrix of the k th sub-triangle, and $\bar{\mathbf{u}}^{(m)}$ is the corresponding displacement vector.

In Eq. (2.31), $\bar{\mathbf{B}}_i$ ($i=1, 2, \dots, l$) denotes the strain-displacement matrices corresponding to the node i located on the target element or neighboring elements, see **Fig. 2.5(a)**. It is noteworthy that the number of components in the strain-displacement matrix and displacement vector is determined by the number of neighboring elements.

Finally, the stiffness matrix of the strain-smoothed polygonal finite element is obtained as follows:

$$\mathbf{K}^{(m)} = \sum_{k=1}^n {}^k \mathbf{K}^{(m)}, \quad (2.32)$$

with

$${}^k \mathbf{K}^{(m)} = \int_{{}^k V^{(m)}} {}^k \bar{\mathbf{B}}^{(m)T} \mathbf{C}^{(m)} {}^k \bar{\mathbf{B}}^{(m)} d {}^k V^{(m)}, \quad (2.33)$$

where ${}^k V^{(m)}$ is the volume of the k th sub-triangle of the element m and $\mathbf{C}^{(m)}$ is the material law matrix for the element m . To calculate the stiffness matrix, three-point Gauss integration is used for each sub-triangle domain.

The proposed polygonal elements are suitable for convex and weakly concave polygonal meshes satisfying the following condition;

$$A_k^{(m)} = \frac{1}{2}(x_c y_{k-1} - x_{k-1} y_c + x_{k-1} y_k - x_k y_{k-1} + x_k y_c - x_c y_k) > 0, \quad (2.34)$$

where $A_k^{(m)}$ is the signed area [35] of the k th sub-triangle of the target element m , and (x_i, y_i) are the coordinates of the three nodal positions of the k th sub-triangle ($i=c, k-1, k$), as shown in **Fig. 2.9**. If the center point is located within the element and the sub-triangles of the element do not overlap each other, the condition is satisfied.

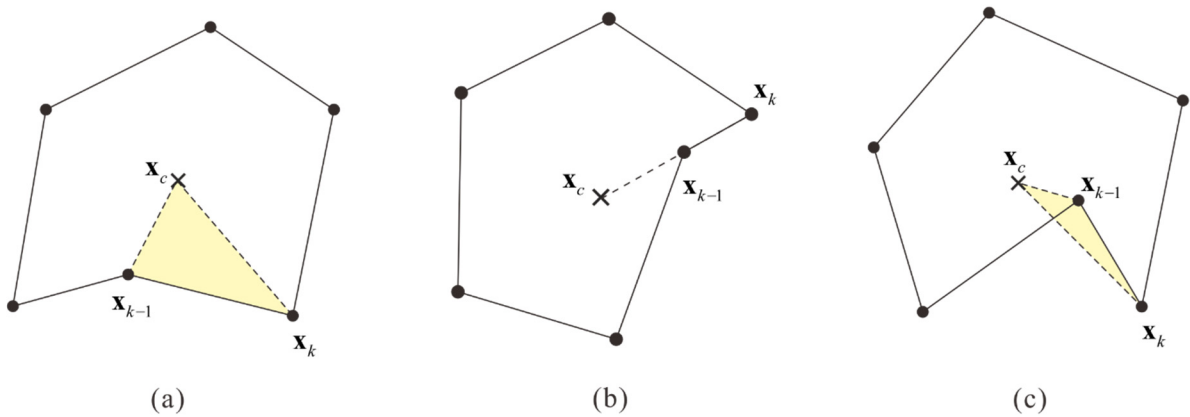


Fig. 2.9. Signed area of a sub-triangle when (a) $A_k^{(m)} > 0$, (b) $A_k^{(m)} = 0$, and (c) $A_k^{(m)} < 0$.

2.3 Basic numerical tests

We conduct basic numerical tests (isotropic element, zero-energy mode, and patch tests) on the strain-smoothed polygonal elements [1].

To pass the isotropy test [38-40], the same response must be obtained for all identical elements with different node numbering sequences, as shown in **Fig. 2.10**. The proposed elements yield the same results regardless of the element node numbering sequences; hence, they pass the isotropic element test.

If no constraint exists on a single 2D solid element, then the stiffness matrix of the element must contain only three zero-energy modes corresponding to the rigid body modes. The zero-energy mode tests are performed using the polygons from triangle to hexagon, as shown in **Fig. 2.11**. The proposed elements pass the zero-energy mode tests.

For the patch tests, the minimum number of DOFs is constrained to prevent rigid body motions, and appropriate loadings are applied to obtain a constant stress field. The same stress value should be obtained at all points on the elements to pass the patch tests. The mesh shown in **Fig. 2.12** is used to perform the normal and shear stress patch tests, and the stress values are obtained from all Gauss integration points. The proposed polygonal elements practically pass the patch tests as shown in **Table 2.1**.

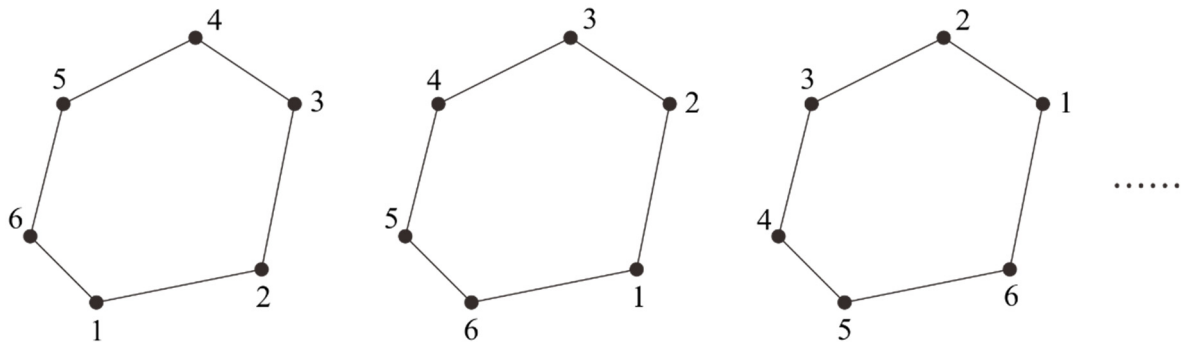


Fig. 2.10. Different node numbering sequences for a polygonal element.

Table 2.1. Minimum and maximum stress values for all Gauss integration points in the patch tests (minimum stress/maximum stress).

| | | σ_{xx} | σ_{yy} | σ_{xy} |
|--------------------------------------|-------------------|------------------|------------------|------------------|
| Normal stress (in x -direction) | Wachspress | 0.99987/1.00010 | -0.00004/0.00004 | -0.00004/0.00009 |
| | Mean value | 0.99973/1.00030 | -0.00011/0.00010 | -0.00023/0.00009 |
| | CS-FEM | 1.00000/1.00000 | -0.00000/0.00000 | -0.00000/0.00000 |
| | ES-FEM | 1.00000/1.00000 | -0.00000/0.00000 | -0.00000/0.00000 |
| | SSE (proposed) | 0.99241/1.00370 | -0.00183/0.00114 | -0.00155/0.00190 |
| | Reference | 1.00000 | 0.00000 | 0.00000 |
| Shear stress | Wachspress | -0.00170/0.00211 | -0.00044/0.00056 | 0.99947/1.00050 |
| | Mean value | -0.00425/0.00322 | -0.00115/0.00092 | 0.99881/1.00100 |
| | CS-FEM | -0.00000/0.00000 | -0.00000/0.00000 | 1.00000/1.00000 |
| | ES-FEM | -0.00000/0.00000 | -0.00000/0.00000 | 1.00000/1.00000 |
| | SSE (proposed) | -0.01404/0.00945 | -0.00819/0.00496 | 0.99488/1.01180 |
| | Reference | 0.00000 | 0.00000 | 1.00000 |

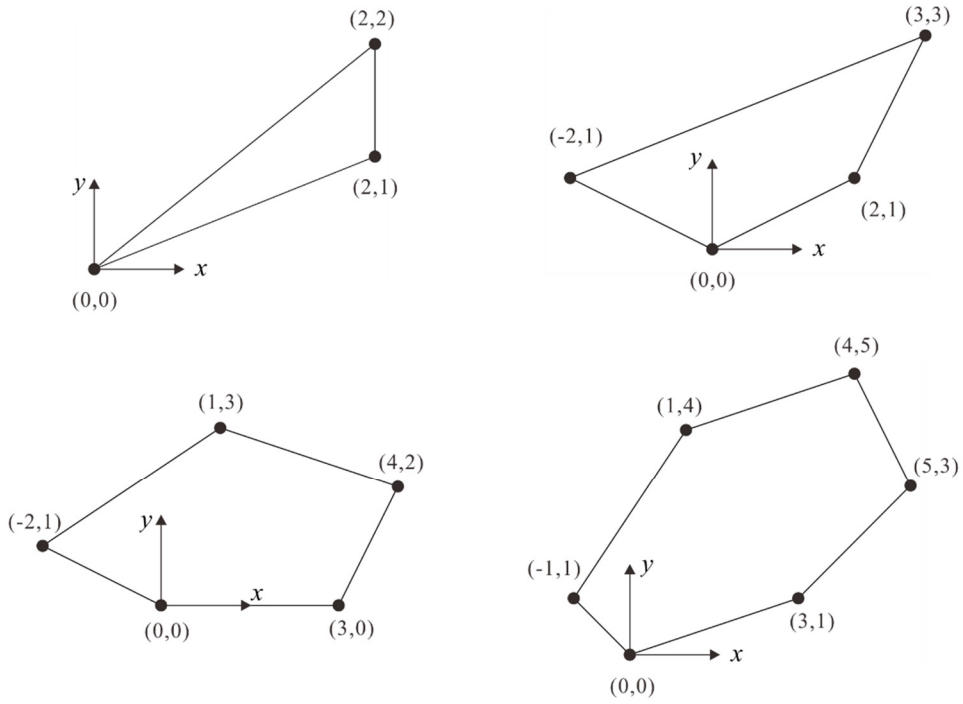


Fig. 2.11. Polygonal meshes used for the zero-energy mode test.

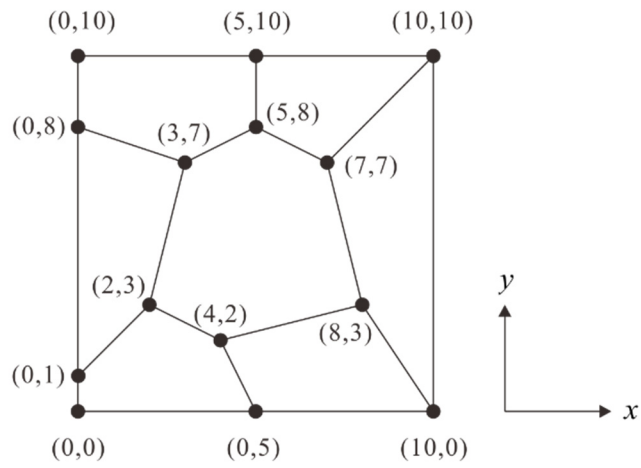


Fig. 2.12. A polygonal mesh used for the patch tests

2.4 Numerical examples

We investigate the performance of the strain-smoothed polygonal finite elements by solving the four numerical examples: an infinite plate with a circular hole, Cook's skew beam, a dam problem, and a ring problem. The unit thickness is considered for all the 2D solid problems.

The performance of the strain-smoothed polygonal finite elements (SSE) is compared with those of the polygonal finite elements based on Wachspress coordinates (Wachspress) [14] and mean value coordinates (Mean value) [15]. In addition, the edge-based smoothed polygonal finite elements (ES-FEM) [28] and the cell-based smoothed polygonal finite elements (CS-FEM) are considered for comparison. The CS-FEMs are segmented into triangular cells for strain smoothing; however, if the polygonal element is a quadrilateral, then this element is segmented into four quadrilateral cells [22,23].

The convergence of the elements is evaluated through their displacements at specific locations and stress distributions. Reference solutions are obtained using sufficiently fine meshes of 9-node quadrilateral finite elements.

The relative error in strain energy E_r is measured as follows:

$$E_r = \frac{|E_{\text{ref}} - E_h|}{E_{\text{ref}}}, \quad (2.35)$$

where E_{ref} is the reference strain energy and E_h is the strain energy calculated from the finite element solutions.

The optimal convergence behavior for linear elements is expressed as

$$E_r \cong ch^2, \quad (2.36)$$

where c is a constant and h is the element size [1].

2.4.1 Infinite plate with a circular hole

We solve the problem of infinite plate with a circular hole shown in **Fig. 2.13** [22,31]. The radius of the circular hole is $a = 1$, and the infinite plate is subjected to a far-field traction $p = 1$ in the x -direction. The plane strain condition is considered with Young's modulus $E = 3 \times 10^7$ and Poisson's ratio $\nu = 0.3$. Owing to symmetry, one-quarter of the plate is modeled as shown in **Fig. 2.13**, and the corresponding boundary conditions are imposed as follows: $u = 0$ along BC and $v = 0$ along AE . **Fig. 2.14** shows meshes used with the total numbers of

elements $N_e = 13, 42, 148, \text{ and } 552$ (or the numbers of elements along the upper edge $N = 2, 4, 8, \text{ and } 16$, respectively). The element size h is defined as $h = 1/N$.

The traction boundary conditions are imposed along CD and DE using the following analytical solutions [35]:

$$\sigma_{xx}(r, \theta) = p \left(1 - \frac{a^2}{r^2} \left(\frac{3}{2} \cos 2\theta + \cos 4\theta \right) + \frac{3a^4}{2r^4} \cos 4\theta \right), \quad (2.37)$$

$$\sigma_{yy}(r, \theta) = p \left(-\frac{a^2}{r^2} \left(\frac{1}{2} \cos 2\theta - \cos 4\theta \right) - \frac{3a^4}{2r^4} \cos 4\theta \right), \quad (2.38)$$

$$\sigma_{xy}(r, \theta) = p \left(-\frac{a^2}{r^2} \left(\frac{1}{2} \sin 2\theta + \sin 4\theta \right) + \frac{3a^4}{2r^4} \sin 4\theta \right), \quad (2.39)$$

where r and θ are the distance from the origin ($x = y = 0$) and counterclockwise angle from the positive x -axis, respectively.

The convergence curves obtained using E_r in Eq. (2.35) are shown in **Fig. 2.15**. The relative errors in the horizontal displacement at point A and the vertical displacement at point B are listed in **Tables 2.2** and **2.3**, respectively. The distributions of the calculated stress component σ_{xy} for the 2.5×2.5 area around the hole are shown in **Fig. 2.16**. The reference solutions are obtained using an 8,192 element mesh of 9-node quadrilateral elements. The proposed elements provide improved convergence behaviors compared with the elements based on Wachspres coordinates and mean value coordinates, the cell-based smoothed elements, and the edge-based smoothed elements.

2.4.2 Cook's skew beam

The well-known Cook's skew beam problem is solved, as shown in **Fig. 2.17** [3]. The left side of the structure is clamped, and a distributed shearing force of total magnitude $P = 1$ is exerted on the right edge. The plane stress condition is assumed with Young's modulus $E = 3 \times 10^7$ and Poisson's ratio $\nu = 0.3$. Solutions are obtained for meshes with the total numbers of elements $N_e = 7, 22, 76, \text{ and } 280$ (or the numbers of elements along the upper edge $N = 2, 4, 8, \text{ and } 16$, respectively), as shown in **Fig. 2.18**. The element size h is defined by $h = 1/N$.

The convergence curves for E_r in Eq. (2.35) are depicted in **Fig. 2.19**. The convergences in the normalized horizontal displacement at point A are shown in **Fig. 2.20**. The relative errors in the horizontal displacement at point A are listed in **Table 2.4**. The reference solutions are obtained using a 64×64 mesh of 9-node quadrilateral elements. Among the polygonal elements considered, the proposed elements provide the best solution accuracy.

The computational efficiency of the considered elements is compared in **Fig. 2.21**. We plot the relations between computation times versus the errors in strain energy. The solutions are obtained using the meshes where the numbers of elements along the upper edge $N = 8, 16, 32, 64,$ and 128 . In addition, a standard 3-node triangular element (named T3) is employed with meshes obtained by triangulation of polygons as shown in **Fig. 2.22**, and the computational efficiency of the T3 element is presented in **Fig. 2.21**. Computations are conducted using a personal computer with Intel Core i7-4790, 3.60GHz CPU, and 8 GB RAM. The skyline solver is used to solve a linear system of equations. As shown in **Fig. 2.21**, the proposed elements give more accurate solutions compared with other elements at similar computation time levels. In other words, the proposed elements exhibit the best computational efficiency among the elements considered in this problem.

2.4.3 Dam problem

A 2D dam structure is subjected to the following surface force on its left edge, as shown in **Fig. 2.23** [39]:

$$f_s = \begin{cases} 5 - y & 0 \leq y \leq 5 \\ (y - 5)^{1/5} & 5 \leq y \leq 10 \end{cases} \quad (2.40)$$

The clamped boundary condition is applied along the bottom edge. The plane strain condition is employed with Young's modulus $E = 3 \times 10^{10}$ and Poisson's ratio $\nu = 0.2$. We use meshes with the total numbers of elements $N_e = 13, 42, 148,$ and 552 , as shown in **Fig. 2.24**. The element size h is $h = 1/N$, where N is the number of elements along the left edge.

The convergence curves are obtained using E_r in Eq. (2.35), as shown in **Fig. 2.25**. The reference solutions are obtained using a 64×128 mesh of 9-node quadrilateral elements. The proposed elements demonstrate significantly improved convergence behaviors compared with the elements based on Wachspress coordinates and mean value coordinates, the cell-based smoothed elements, and the edge-based smoothed elements.

In addition, we evaluate the performance of the proposed elements for meshes constructed using the paving and cutting algorithm. Using the meshing algorithm, the interior of the problem domain is uniformly meshed for quadrilateral elements, but the boundary is meshed for polygonal elements [5-8]. **Fig. 2.26** shows the resulting meshes obtained by using the meshing algorithm for this problem. The uniform grid sizes used are $h_{\text{grid}} = 2, 0.8, 0.4,$ and 0.2 . For convergence studies, the element size h is defined as $h = 1/N$, with an equivalent number of elements $N = L_c/h_{\text{grid}}$ (characteristic length $L_c = 10$ in this problem). **Fig. 2.27** shows the convergence curves obtained using E_r in Eq. (2.35). The proposed elements provide improved solution accuracy, even when used with the paving and cutting algorithm.

2.4.4 Ring problem

A 2D ring structure is subjected to a surface force in the direction normal to the surface as shown in **Fig. 2.28**. For this symmetric problem, one quarter of the ring is considered with the following boundary conditions: $u = 0$ along AB , and $v = 0$ along CD , as shown in **Fig. 2.28**. The plane stress condition is assumed with Young's modulus $E = 3 \times 10^3$ and Poisson's ratio $\nu = 0.3$.

As shown in **Fig. 2.29**, meshes with the total numbers of elements $N_e = 16, 56,$ and 205 are obtained by using the paving and cutting algorithm. Here, the uniform grid sizes are $h_{\text{grid}} = 1/2, 1/4,$ and $1/8$ of the ring width $L_c = 2$. The element size h is defined as $h = 1/N$, with an equivalent number of elements $N = L_c/h_{\text{grid}}$.

The convergence curves for E_r in Eq. (2.35) are shown in **Fig. 2.30**. The von Mises stress distributions are shown in **Fig. 2.31**. The convergences in the normalized vertical displacement at point A are shown in **Fig. 2.32**. The relative errors in the vertical displacement at point A are listed in **Table 2.5**. The reference solutions are obtained using a 64×64 mesh of 9-node quadrilateral elements. The proposed elements demonstrate significantly better convergence behaviors than the other elements considered.

In all the numerical examples presented, the proposed elements consistently yield better convergence behaviors compared with the elements using Wachspress shape functions, the cell-based smoothed elements, and the edge-based smoothed elements. Additionally, the proposed elements are effective when used with the paving and cutting algorithm.

Table 2.2. Relative errors in the horizontal displacement ($|u_{\text{ref}} - u_h|/u_{\text{ref}} \times 100$) at point A in the infinite plate with a circular hole.

| N_e | Wachspress | Mean value | CS-FEM | ES-FEM | SSE (proposed) |
|---|------------|------------|--------|--------|----------------|
| 13 | 12.831 | 13.566 | 19.302 | 16.419 | 6.324 |
| 42 | 8.666 | 9.023 | 11.862 | 7.517 | 2.898 |
| 148 | 5.694 | 5.913 | 7.442 | 2.604 | 0.729 |
| 552 | 3.317 | 3.479 | 4.459 | 0.631 | 0.022 |
| Reference solution: $u_{\text{ref}} = 9.101 \times 10^{-8}$ | | | | | |

Table 2.3. Relative errors in the vertical displacement ($|v_{\text{ref}} - v_h|/v_{\text{ref}} \times 100$) at point B in the infinite plate with a circular hole.

| N_e | Wachspress | Mean value | CS-FEM | ES-FEM | SSE (proposed) |
|--|------------|------------|--------|--------|----------------|
| 13 | 19.143 | 19.304 | 21.998 | 16.798 | 14.139 |
| 42 | 16.809 | 17.156 | 19.225 | 10.158 | 8.187 |
| 148 | 13.117 | 13.530 | 15.748 | 4.200 | 2.641 |
| 552 | 8.387 | 8.785 | 10.896 | 1.029 | 0.428 |
| Reference solution: $v_{\text{ref}} = -3.034 \times 10^{-8}$ | | | | | |

Table 2.4. Relative errors in the horizontal displacement ($|u_{\text{ref}} - u_h|/u_{\text{ref}} \times 100$) at point A in Cook's skew beam problem.

| N_e | Wachspress | Mean value | CS-FEM | ES-FEM | SSE (proposed) |
|--|------------|------------|--------|--------|----------------|
| 7 | 61.270 | 62.422 | 68.968 | 44.119 | 25.828 |
| 22 | 33.579 | 34.823 | 42.504 | 12.452 | 6.089 |
| 76 | 14.478 | 15.140 | 19.537 | 4.681 | 2.710 |
| 280 | 5.879 | 6.136 | 7.879 | 2.127 | 1.301 |
| Reference solution: $u_{\text{ref}} = -6.301 \times 10^{-7}$ | | | | | |

Table 2.5. Relative errors in the vertical displacement ($|v_{\text{ref}} - v_h| / v_{\text{ref}} \times 100$) at point A in the ring problem.

| N_e | Wachspress | Mean value | CS-FEM | ES-FEM | SSE (proposed) |
|-------|------------|------------|--------|--------|----------------|
| 16 | 99.953 | 101.652 | 74.198 | 79.101 | 8.186 |
| 56 | 31.261 | 32.001 | 22.724 | 23.946 | 2.754 |
| 205 | 8.337 | 8.549 | 5.687 | 5.568 | 0.447 |

Reference solution: $v_{\text{ref}} = 5.996 \times 10^{-4}$

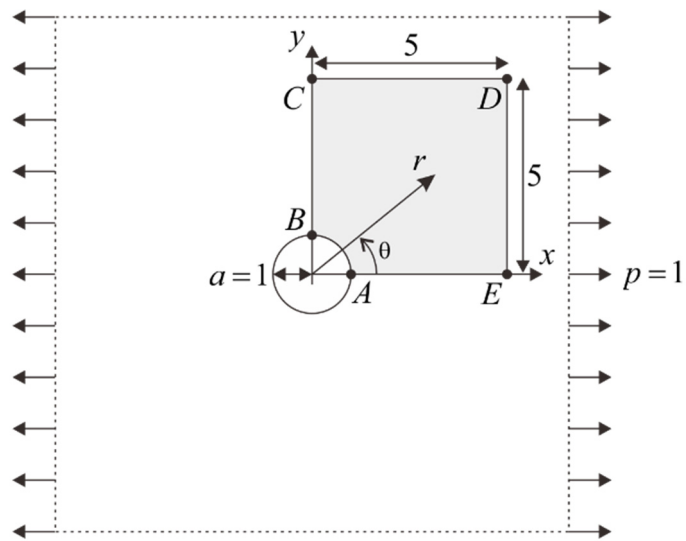


Fig. 2.13. Infinite plate with a circular hole ($E = 3 \times 10^7$ and $\nu = 0.3$). Only shaded domain is meshed due to symmetry.

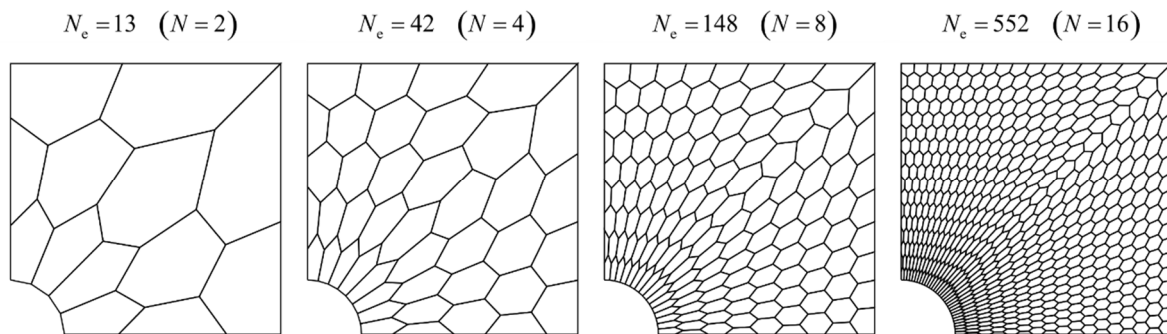


Fig. 2.14. Polygonal meshes used for the infinite plate with a circular hole.

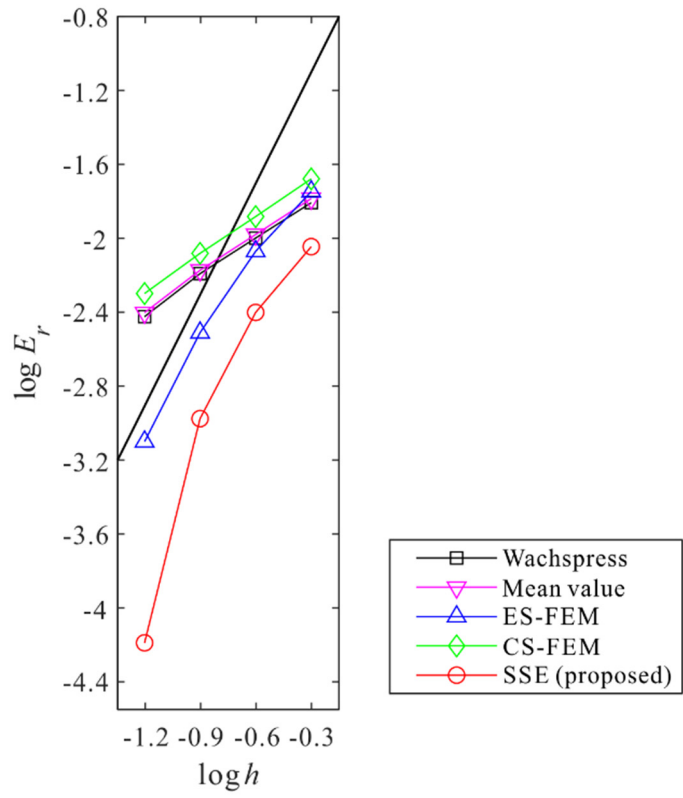


Fig. 2.15. Convergence curves for the infinite plate with a circular hole. The bold line represents the optimal convergence rate.

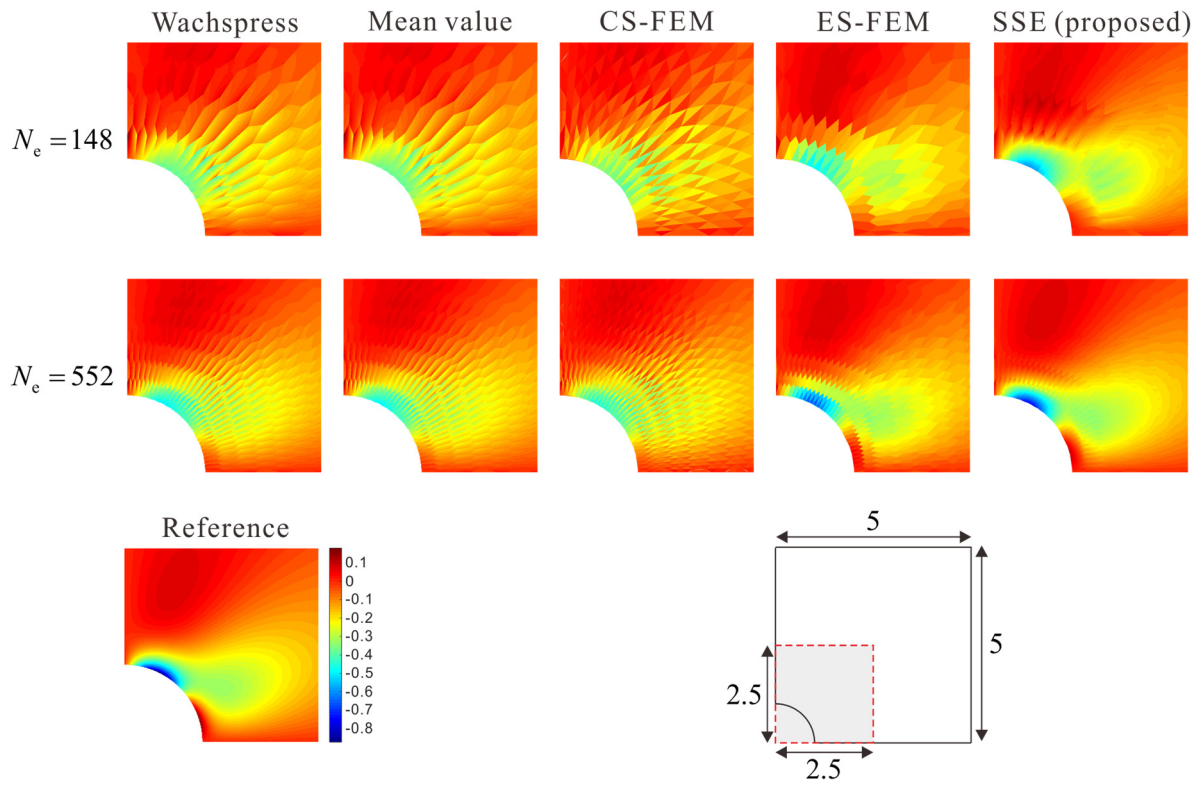


Fig. 2.16. Stress distributions (σ_{yy}) for the infinite plate with a circular hole. Only 2.5×2.5 area around the hole is plotted. The reference stress distribution is obtained using an 8,192 element mesh of 9-node quadrilateral elements.

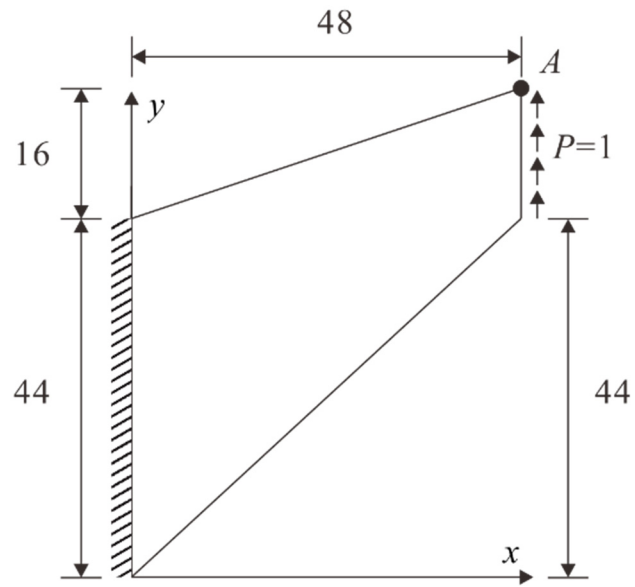


Fig. 2.17. Cook's skew beam ($E = 3 \times 10^7$ and $\nu = 0.3$).

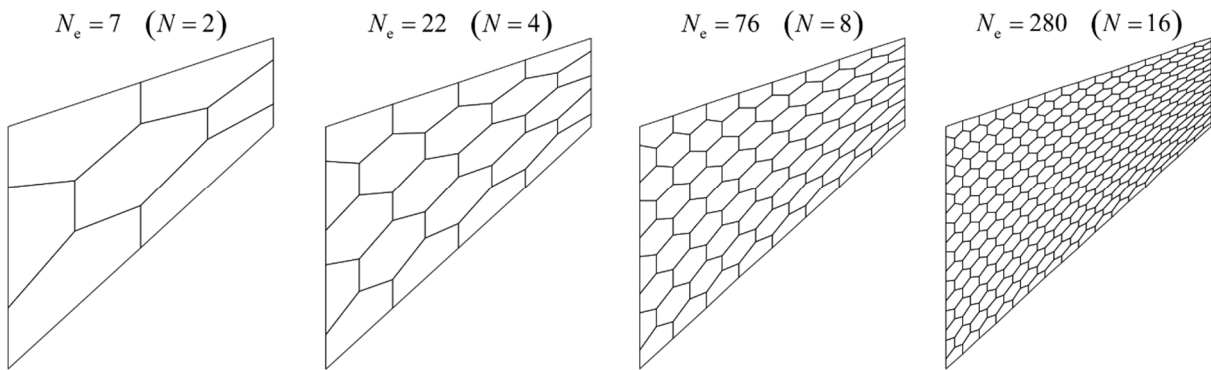


Fig. 2.18. Polygonal meshes used for Cook's skew beam.

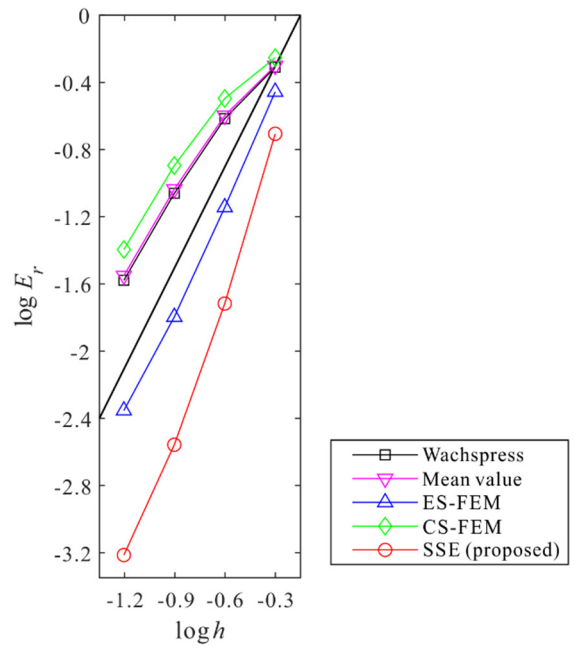


Fig. 2.19. Convergence curves for Cook's skew beam. The bold line represents the optimal convergence rate.

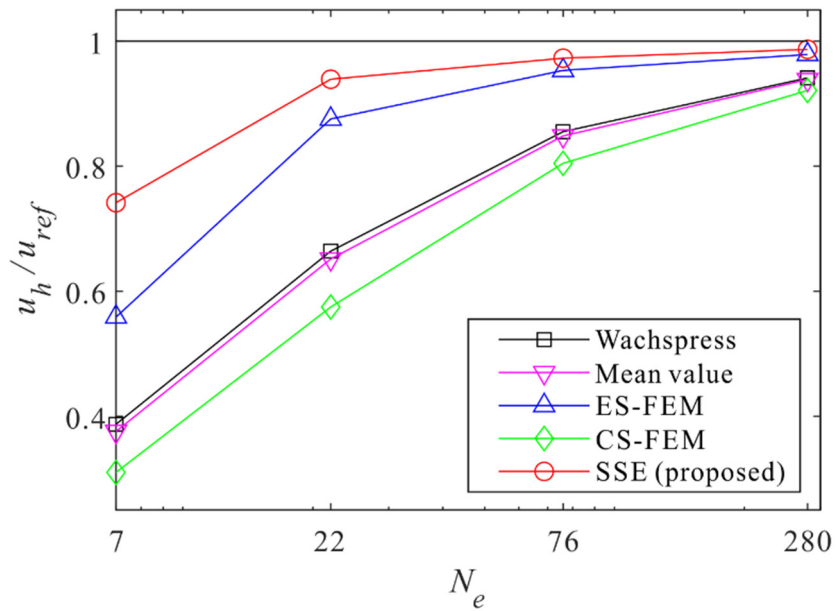


Fig. 2.20. Normalized horizontal displacements (u_h/u_{ref}) at point A in Cook's skew beam.

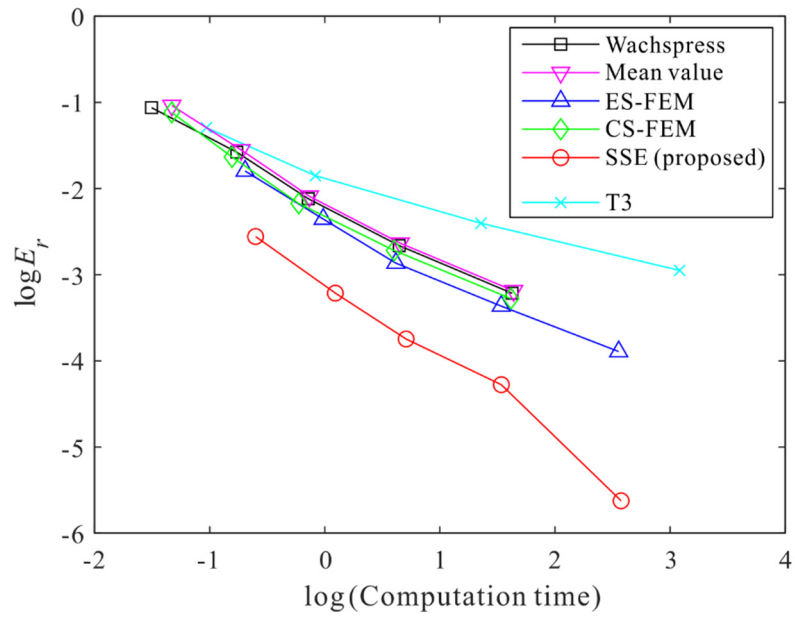


Fig. 2.21. Computational efficiency curves for Cook's skew beam. The computation times are measured in seconds.

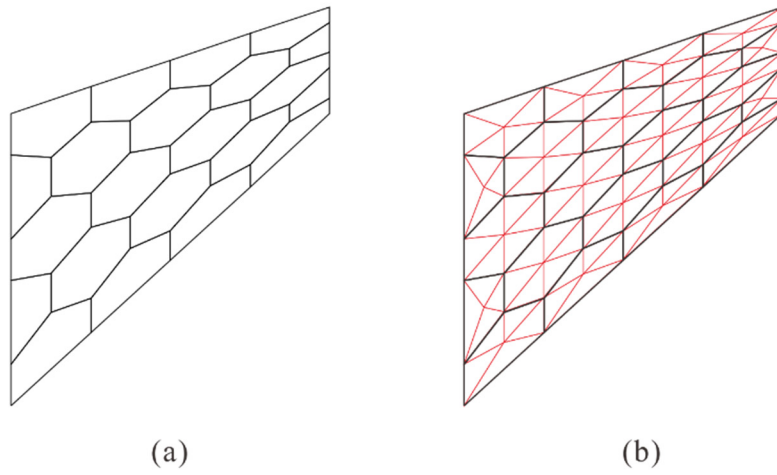


Fig. 2.22. Mesh obtained by triangulation of polygons ($N = 4$): (a) Polygonal mesh (92 DOFs). (b) Triangular mesh (136 DOFs).

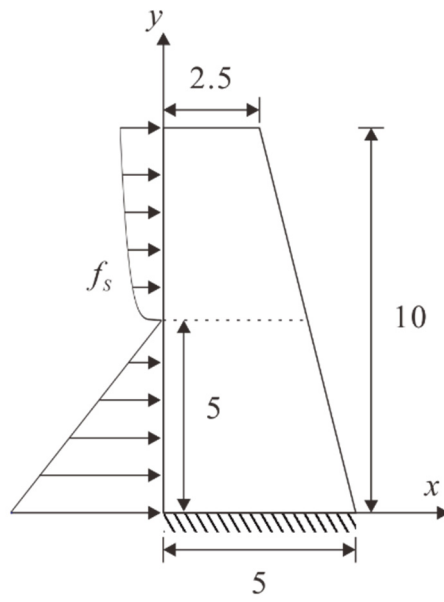
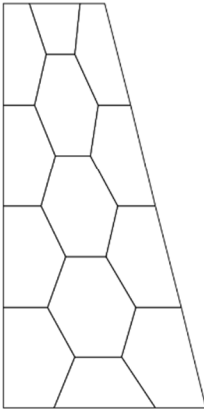
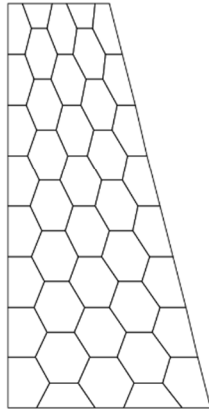


Fig. 2.23. Dam problem ($E = 3 \times 10^{10}$ and $\nu = 0.2$).

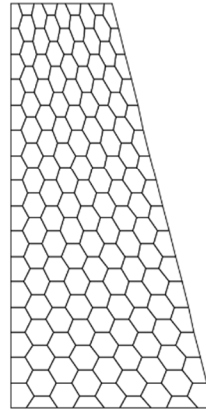
$N_e = 13$ ($N = 4$)



$N_e = 42$ ($N = 8$)



$N_e = 148$ ($N = 16$)



$N_e = 552$ ($N = 32$)

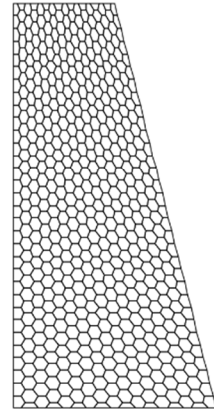


Fig. 2.24. Polygonal meshes used for the dam problem.

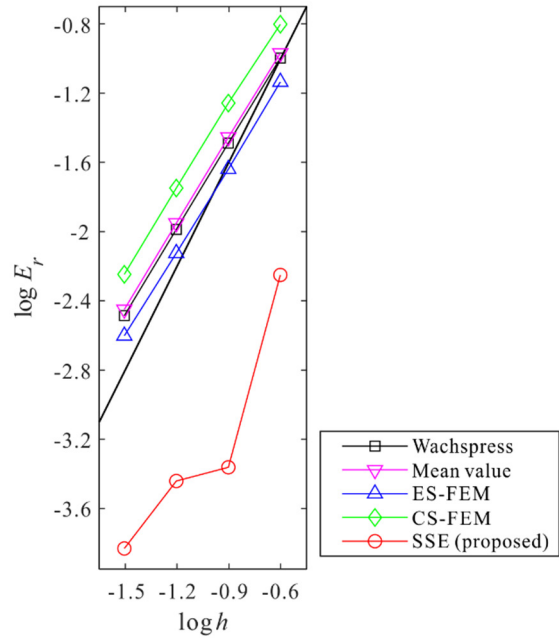


Fig. 2.25. Convergence curves for the dam problem. The bold line represents the optimal convergence rate.

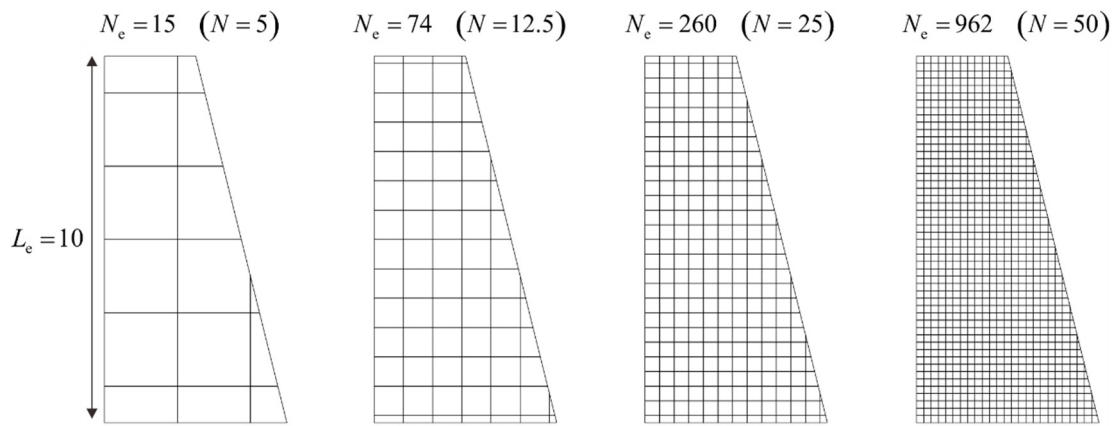


Fig. 2.26. Polygonal meshes constructed using the paving and cutting algorithm for the dam problem.

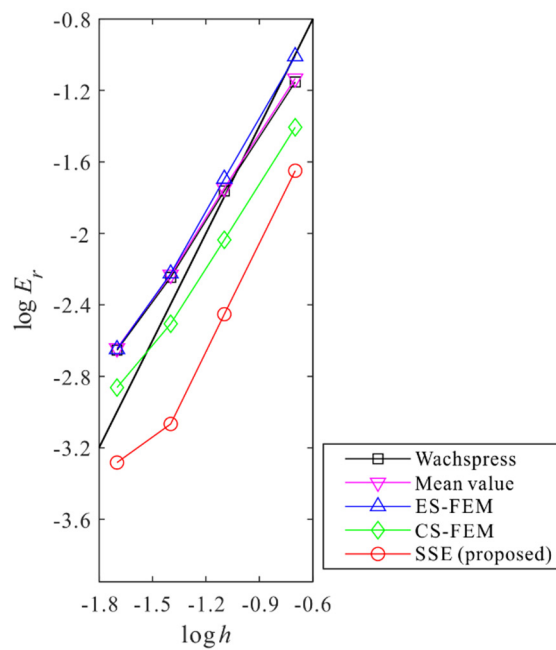


Fig. 2.27. Convergence curves for the dam problem when the meshes with the paving and cutting algorithm are utilized. The bold line represents the optimal convergence rate.

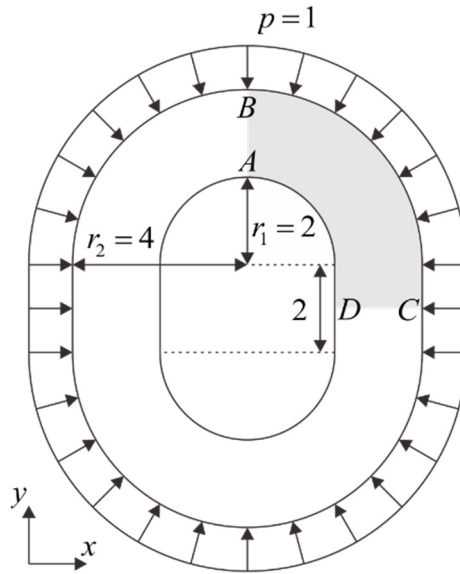


Fig. 2.28. Ring problem ($E = 3 \times 10^3$ and $\nu = 0.3$). Only shaded domain is considered for analysis owing to symmetry.

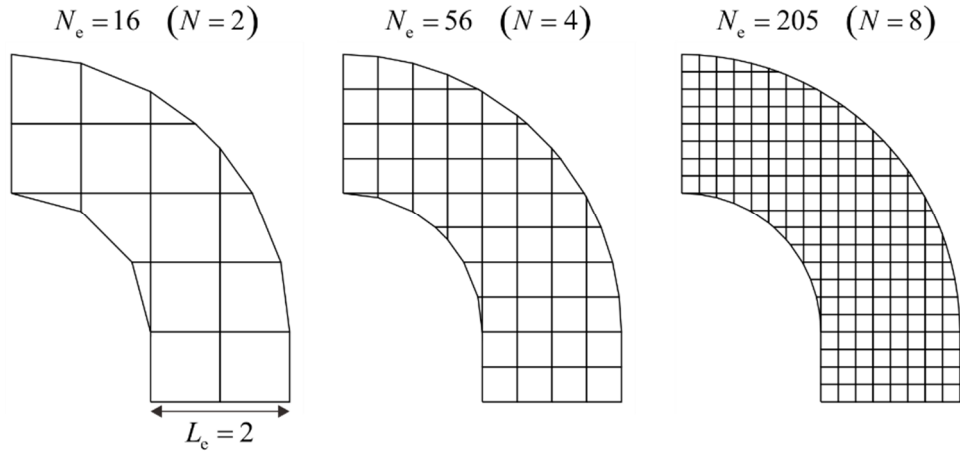


Fig. 2.29. Polygonal meshes constructed using the paving and cutting algorithm for the ring problem.

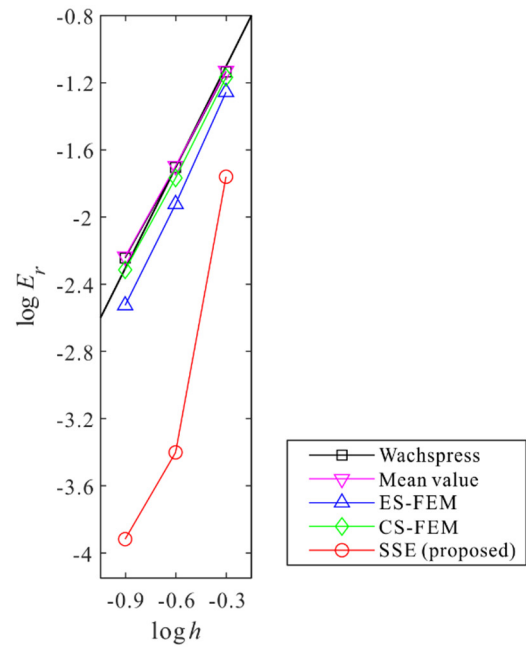


Fig. 2.30. Convergence curves for the ring problem. The bold line represents the optimal convergence rate.

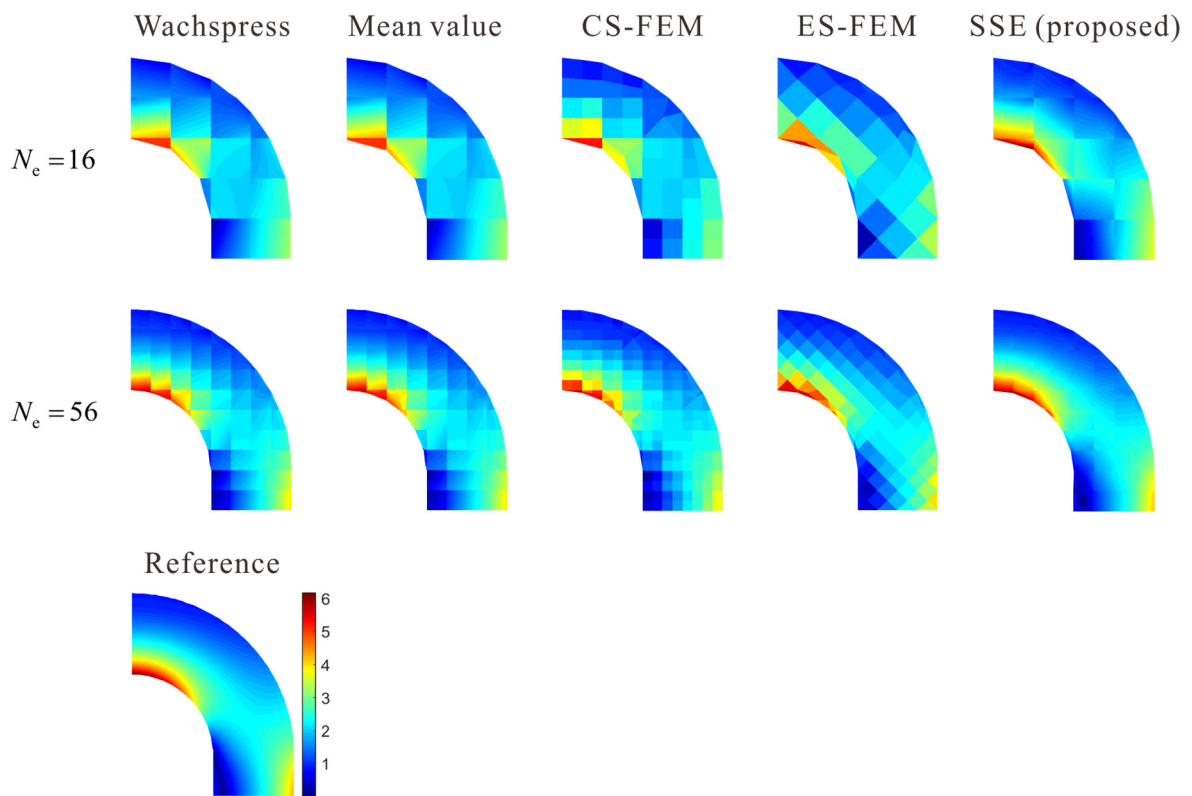


Fig. 2.31. von Mises stress distributions for the ring problem. The reference stress distribution is obtained using a 64×64 mesh of 9-node quadrilateral elements.

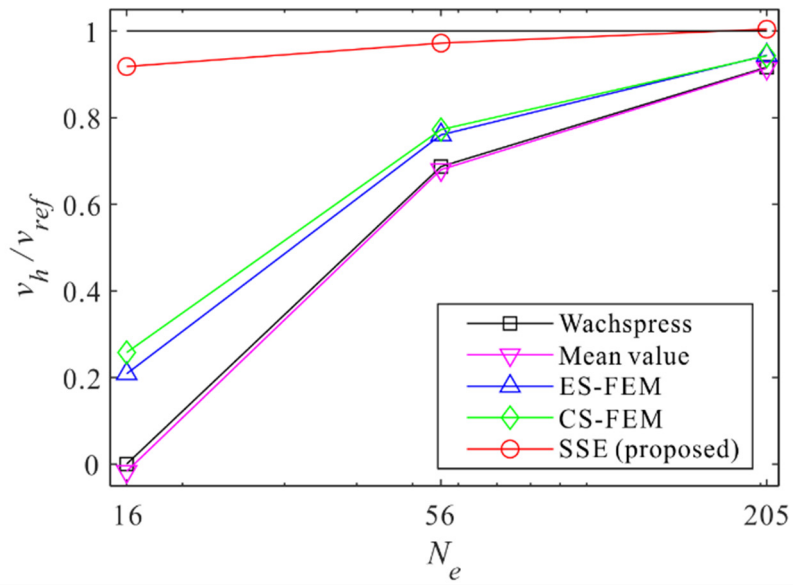


Fig. 2.32. Normalized vertical displacements (v_h/v_{ref}) at point A in the ring problem.

Chapter 3. Volumetric locking alleviation in the strain-smoothed 3-node triangular finite element

Volumetric locking is a phenomenon that occurs when an object approaches incompressibility. In this situation, the bulk modulus takes an exceedingly large value, and the volume change of the object has an extremely small value. In situations of volumetric locking, the volume tends to appear almost uniformly at all integration points, often leading to computations that seem to involve an excessive number of integration points compared to the variables in the problem. To address this, volumetric locking is often resolved by reducing the number of integration points or increasing the variables by adding degrees of freedom [1-3,40-42,45].

The 3-node triangular finite element is one of the most traditional elements and is still widely used today. However, the 3-node element has a problem where the strain field within the element is constant, making it impossible to alleviate volumetric locking with reduced integration. Various mixed formulations have been proposed to address volumetric locking; however, applying them to 3-node elements has been challenging due to the lower order of interpolation functions of a 3-node triangular element or often involves an increase in degrees of freedom.

Strain smoothing techniques have been developed to improve elements without increasing degrees of freedom, and these techniques have been extensively applied in solid elements. Despite their benefits, these techniques confront issues associated with volumetric locking. Node-based smoothed finite element method is known for being immune to volumetric locking [25]; However, it tends to produce somewhat softened solutions, impacting the competitiveness of element performance. The strain-smoothed element method establishes a smoothed strain field within the element without creating a distinct smoothing domain, demonstrating improved performance compared to other strain smoothing techniques. While volumetric locking has been effectively addressed in 4-node quadrilateral strain-smoothed element [33], the challenge persists in the 3-node triangular strain-smoothed element due to the lower order of interpolation functions, making it impossible to address locking in the same manner.

In this chapter, volumetric locking alleviation techniques are introduced and the new techniques are proposed for the strain-smoothed 3-node triangular element. To alleviate the volumetric locking, deviatoric strain and volumetric strain are calculated separately. The deviatoric strain field is formed within the element through integration points in the element using the SSE method. The smoothed volumetric strain is calculated for each node by utilizing the strains assigned at integration points positioned in close to the node. Eventually, a linear strain field is established based on the smoothed volumetric strains in the nodes.

We briefly introduce volumetric locking and present the formulation of the strain-smoothed 3-node triangular finite elements to alleviate volumetric locking.

3.1 Volumetric locking in 2D solid elements

Volumetric locking is commonly observed in the analysis of nearly incompressible materials, where the unphysically stiff analysis results are obtained as the Poisson's ratio approaches 0.5 (incompressible condition). To examine the physical and numerical meanings of volumetric locking, let's consider the definition of the bulk modulus. In the situation depicted in **Fig. 3.1**, the relationship between pressure and volume change is as follows;

$$\Delta P = -\kappa \frac{\Delta V}{V}, \quad (3.1)$$

or

$$p = -\kappa^{vol} \varepsilon, \quad (3.2)$$

where κ is bulk modulus, P is hydrostatic pressure, p is hydrostatic stress, V is initial volume, ΔV is volume change and ${}^{vol} \varepsilon$ is volumetric strain.

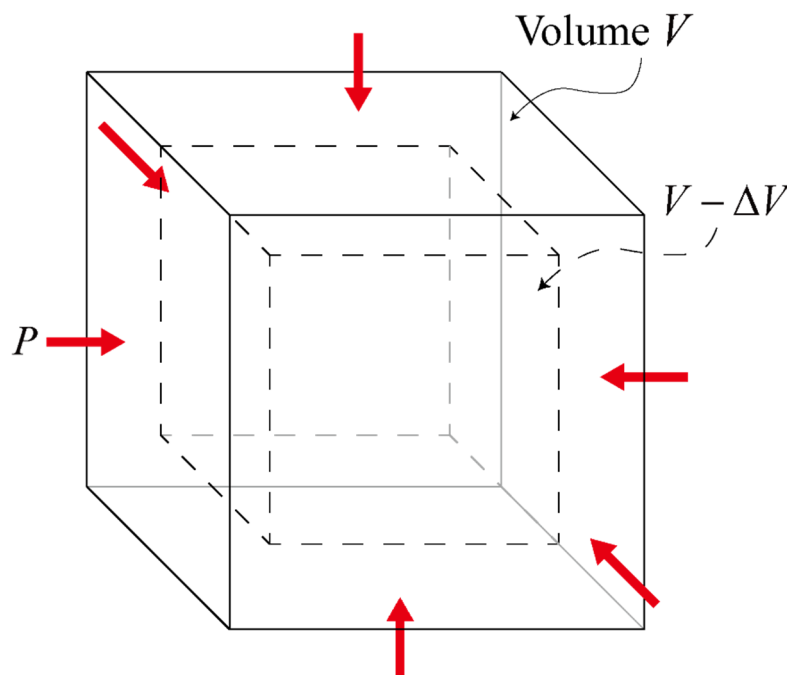


Fig. 3.1. Hydrostatic pressure and volume change.

Volumetric locking occurs in situations where there is nearly incompressible behavior, meaning the bulk modulus is extremely large. Simultaneously, as the volume undergoes almost no change, the volumetric strain should have a very small value. This situation can generate significant errors in stress and displacement even with small errors

in volumetric strain. When the interpolation functions fail to adequately describe such extremely small volumetric strains, errors can occur in the estimation of volumetric strain.

Additionally, due to the extremely small changes in volume, the volume remains nearly constant across all integration points. This situation results in analyses that seem to use an excessive number of integration points in comparison to the variables involved in the problem. To address such over-constraint situation, it is commonly practiced to reduce the number of integration points or increase the number of variables to augment degrees of freedom.

In order to address volumetric locking, the formulation is described by separating into independent volumetric and deviatoric terms. Most mixed formulations are applied to the separated volumetric term [2,40].

In the case of 2D solid elements, the volumetric strain ${}^{vol}\boldsymbol{\varepsilon}$ induced by volume change is defined as follows:

$${}^{vol}\boldsymbol{\varepsilon} = \frac{\Delta V}{V} = \boldsymbol{\varepsilon}_{xx} + \boldsymbol{\varepsilon}_{yy} = {}^{vol}\mathbf{B}\mathbf{u}, \quad (3.3)$$

and the deviatoric strain ${}^{dev}\boldsymbol{\varepsilon}_{ij}$ is obtained as follows:

$${}^{dev}\boldsymbol{\varepsilon}_{ij} = \boldsymbol{\varepsilon}_{ij} - \frac{1}{2} {}^{vol}\boldsymbol{\varepsilon} \delta_{ij} = {}^{dev}\mathbf{B}_{ij}\mathbf{u}, \quad (3.4)$$

where ${}^{vol}\mathbf{B}$ and ${}^{dev}\mathbf{B}_{ij}$ are the strain-displacement matrices (component) for the volumetric strain ${}^{vol}\boldsymbol{\varepsilon}$ and deviatoric strain ${}^{dev}\boldsymbol{\varepsilon}_{ij}$, respectively, δ_{ik} is the Kronecker delta, and \mathbf{u} is the nodal displacement vector.

Then, the stiffness matrix \mathbf{K} is calculated using the strain-displacement matrices ${}^{vol}\mathbf{B}$ and ${}^{dev}\mathbf{B}$ as

$$\mathbf{K} = \int_V ({}^{vol}\mathbf{B} + {}^{dev}\mathbf{B})^T \mathbf{C} ({}^{vol}\mathbf{B} + {}^{dev}\mathbf{B}) dV, \quad (3.5)$$

where \mathbf{C} is the material law matrix.

Due to the independence of ${}^{vol}\mathbf{B}$ and ${}^{dev}\mathbf{B}$, Eq. (3.5) is expressed as

$$\mathbf{K} = \int_V \left(\kappa + \frac{\eta}{3} G \right) {}^{vol}\mathbf{B}^T {}^{vol}\mathbf{B} dV + \int_V {}^{dev}B_{ij} C_{ij}^{dev} {}^{dev}B_{ij} dV = \mathbf{K}^{vol} + \mathbf{K}^{dev}, \quad (3.6)$$

where $\eta = \frac{(1+\nu)(1-4\nu)}{(1-\nu)(1-2\nu)}$ for the plane stress condition, $\eta = 1$ for the plane strain condition, κ is bulk modulus, G is shear modulus, and C_{ij}^{dev} represents the material law tensor for deviatoric strain and stress, as

expressed follows: $C_{11}^{dev} = C_{22}^{dev} = 2G$ and $C_{12}^{dev} = G$.

In the plane strain condition, the material properties κ and G can be expressed as a function of the Poisson's ratio as follows:

$$\kappa = \frac{E}{3(1-2\nu)} \quad \text{and} \quad G = \frac{E}{2(1+\nu)}, \quad (3.7)$$

where E is Young's modulus. As the Poisson's ratio approaches 0.5, the bulk modulus increases significantly. When errors arise in the description of strain-displacement matrix due to interpolation functions, this leads to the creation of an excessively stiff volumetric stiffness matrix \mathbf{K}^{vol} . Accordingly, reduced integration over the volumetric term or assuming a constant strain field can be employed to alleviate volumetric locking.

For the 4-node quadrilateral finite element, reduced integration to address volumetric locking is performed as shown in **Fig. 3.2**. The strains and stiffness matrices are defined as bilinear functions within the field, and to alleviate the volumetric locking, the number of integration points in the volumetric term is reduced for computation. By reducing the number of integration points, the volumetric strain field is assumed to be constant. However, in the case of 3-node triangular element, where strain remains constant within the element, reduced integration cannot be applied.

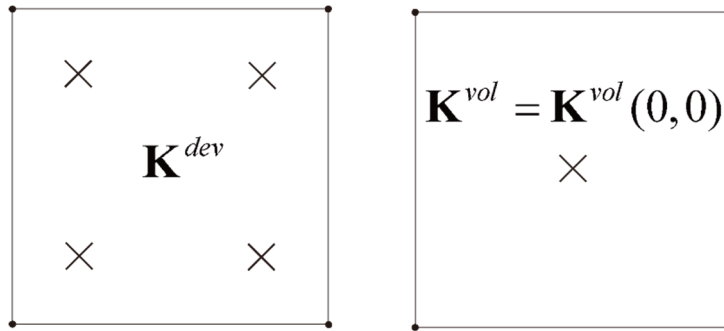


Fig. 3.2. Integration points for the deviatoric and volumetric term in the 4-node quadrilateral finite element.

3.1.1 Treatment of volumetric locking in the strain-smoothed elements

The strain-smoothed element method has been applied to various 2D solid elements, including 3-node triangular, 4-node quadrilateral, even polygonal elements, improving the performance of elements. The strain-smoothed elements may also encounter volumetric locking. To address this, for the 4-node quadrilateral element, a treatment has been proposed that assumes a constant strain field for the volumetric strain [33].

As shown in **Fig. 3.3**, smoothed strains based on the edge and smoothed strains in the Gauss integration points are defined from Eq. 2.11 and 2.12. Based on these smoothed strains, the constant volumetric strain is assumed as follows:

$$\text{vol } \bar{\boldsymbol{\varepsilon}}^{(m)} = \frac{1}{A^{(m)}} \sum_{k=1}^4 A_k^{(m)} (\hat{\boldsymbol{\varepsilon}}_{11}^{(k)} + \hat{\boldsymbol{\varepsilon}}_{22}^{(k)}) = \text{vol } \bar{\mathbf{B}}^{(m)} \bar{\mathbf{u}}^{(m)}, \quad (3.8)$$

and the deviatoric strain is defined as

$$\text{dev } \bar{\boldsymbol{\varepsilon}}_{ij}^{(m)} = \bar{\boldsymbol{\varepsilon}}_{ij}^{(m)} - \frac{1}{2} \text{vol } \bar{\boldsymbol{\varepsilon}}^{(m)} \delta_{ij} = \text{dev } \bar{\mathbf{B}}_{ij}^{(m)} \bar{\mathbf{u}}^{(m)}. \quad (3.9)$$

As shown in **Fig. 3.3** (b) and (c), the deviatoric strain is allocated at integration points, forming a linear strain field within the element, and volumetric strain is applied uniformly within the element.

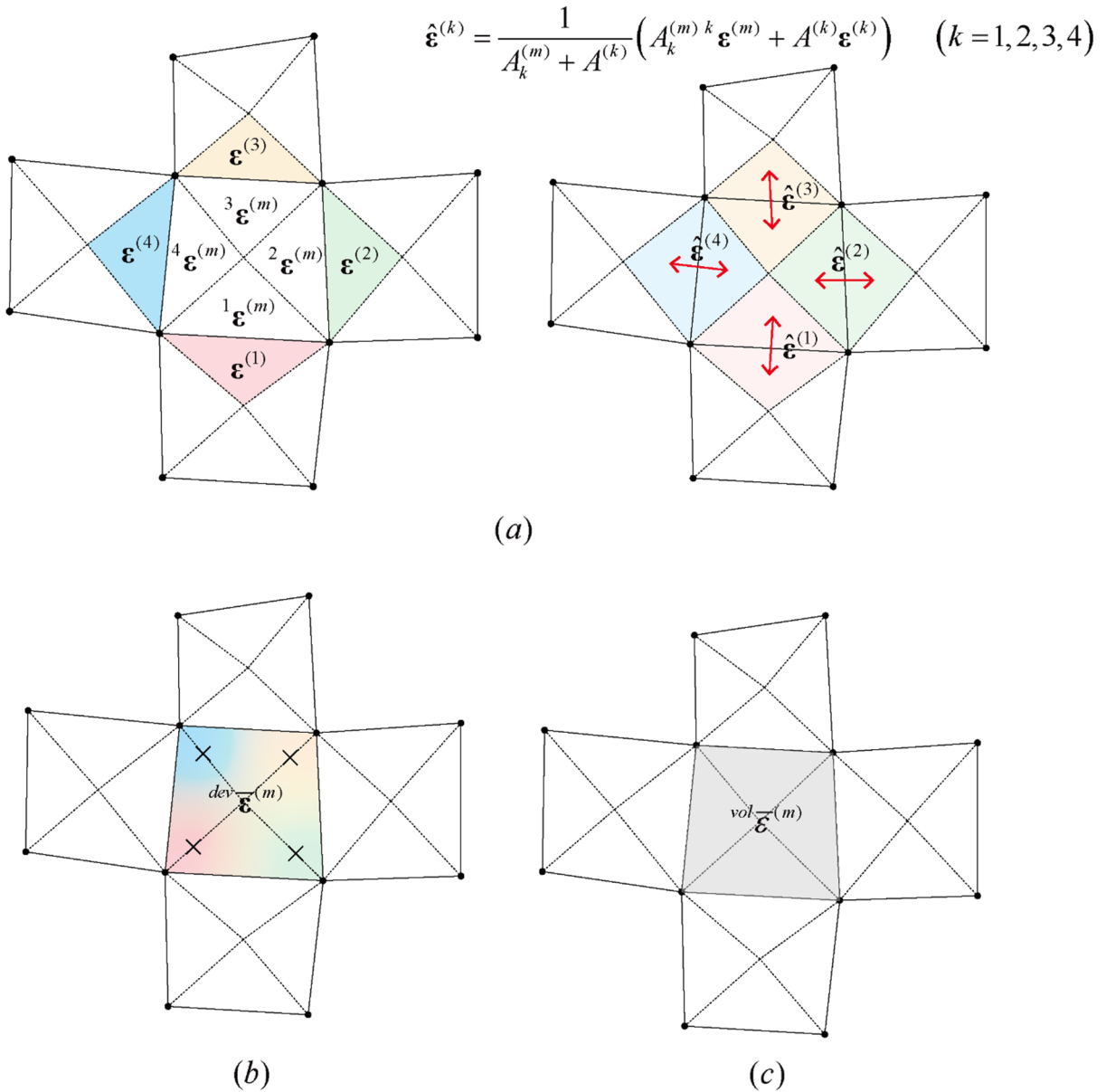


Fig. 3.3. The 4-node strain-smoothed element: (a) smoothed strain through the edges, (b) a deviatoric strain field, (c) a constant volumetric strain field.

The definition of volumetric strain can be similarly applied not only to 4-node quadrilateral element but also to polygonal elements as shown in **Fig. 3.4**. For n -sided polygonal element m , the constant volumetric strain ${}^{vol}\boldsymbol{\varepsilon}^{(m)}$ is defined as follows:

$${}^{vol}\boldsymbol{\varepsilon}^{(m)} = \frac{1}{A^{(m)}} \sum_{k=1}^n A_k^{(m)} \left(\hat{\boldsymbol{\varepsilon}}_{11}^{(k)} + \hat{\boldsymbol{\varepsilon}}_{22}^{(k)} \right), \quad (3.10)$$

where $\hat{\boldsymbol{\varepsilon}}^{(k)}$ is the smoothed strain between the k th sub-triangle of the target element m and its adjacent sub-triangle of the neighboring element.

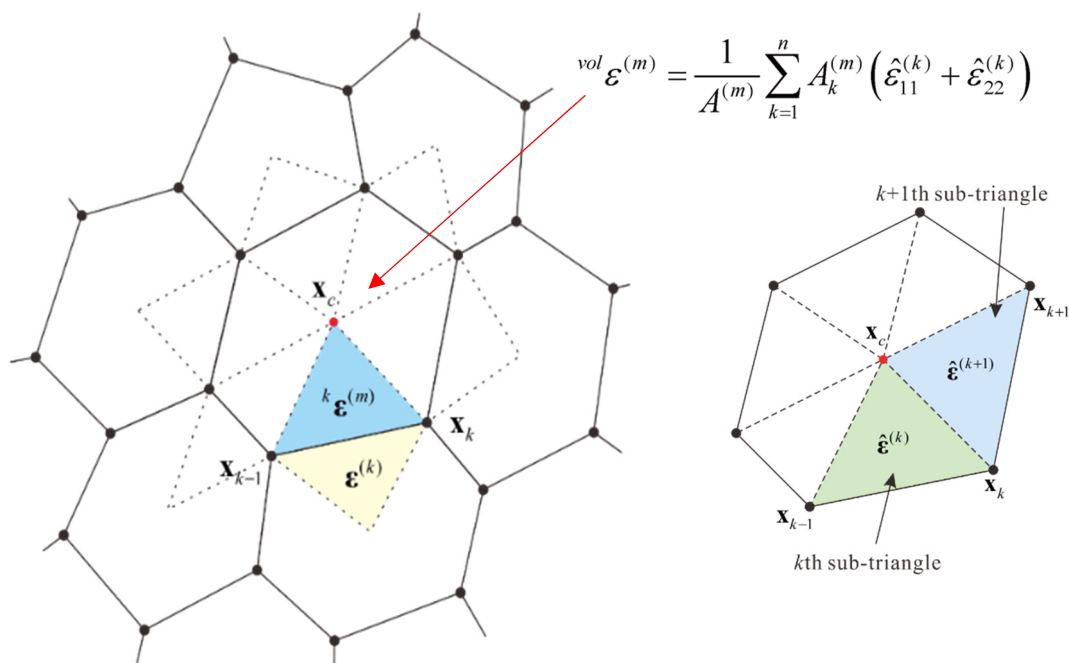


Fig. 3.4. The assumed volumetric strain in the strain-smoothed polygonal finite element.

Even though the 3-node triangular strain-smoothed element forms a linear strain field similarly to the 4-node quadrilateral strain-smoothed element, applying constant volumetric strain in the same way as mentioned before does not alleviate volumetric locking.

3.2 Formulation of the strain-smoothed 3-node triangular finite element to alleviate volumetric locking

As introduced in Chapter 3.1, the strain and stiffness matrix are separately computed into deviatoric and volumetric terms, and constant strain field is assumed to the volumetric term. However, in the case of 3-node triangular element, it features a constant strain field and stiffness matrix, which means that softened results cannot be achieved through the reduced integration (or assumed constant volumetric strain). While the SSE method can establish a linear strain field within the element, applying constant volumetric strain cannot effectively mitigate volumetric locking. In this part, we introduce the separation of deviatoric and volumetric terms of the smoothed strain and present approaches for alleviating volumetric locking by addressing the volumetric term.

3.2.1 Strain-smoothed element method for deviatoric strain

It has been introduced in Chapter 2.1 regarding the formulation of the strain-smoothed 3-node triangular element. From Eq. (2.6) and **Fig. 2.1**, the smoothed strains $\bar{\boldsymbol{\varepsilon}}_k$ are assigned to integration points in the element. Similar to Eq. (3.1) and (3.2), the smoothed strain $\bar{\boldsymbol{\varepsilon}}_k$ is separated into volumetric and deviatoric terms as follows:

$${}^{vol}\bar{\boldsymbol{\varepsilon}}_k = (\bar{\boldsymbol{\varepsilon}}_k)_{11} + (\bar{\boldsymbol{\varepsilon}}_k)_{22} = {}^{vol}\bar{\mathbf{B}}_k \bar{\mathbf{u}}^{(m)}, \quad (3.10)$$

$${}^{dev}(\bar{\boldsymbol{\varepsilon}}_k)_{ij} = (\bar{\boldsymbol{\varepsilon}}_k)_{ij} - \frac{1}{2} {}^{vol}\bar{\boldsymbol{\varepsilon}}_k \delta_{ij} = {}^{dev}(\bar{\mathbf{B}}_k)_{ij} \bar{\mathbf{u}}^{(m)} \quad \text{with } k = 1, 2, 3, \quad (3.11)$$

where ${}^{vol}\bar{\mathbf{B}}_k$ and ${}^{dev}(\bar{\mathbf{B}}_k)_{ij}$ are strain-displacement matrices (component) relating the volumetric and deviatoric strains of the smoothed strain $\bar{\boldsymbol{\varepsilon}}_k$ to the displacement vector $\bar{\mathbf{u}}^{(m)}$ for the target element m . Note that the length of the displacement vector varies according to the number of neighboring elements.

Subsequently, \mathbf{K}^{dev} , i.e., the stiffness matrix for deviatoric strain is computed through three integration points within the triangular element. Note that the smoothed strain field obtained through the SSE method is linearly represented within the 3-node triangular element, but volumetric locking cannot be alleviated by simply applying constant volumetric stiffness matrix \mathbf{K}^{vol} . As shown in **Fig. 3.5**, The field of smoothed strain within the triangular element can be expressed as

$$\bar{\boldsymbol{\varepsilon}}(r, s) = \left[1 - \frac{1}{q-p}(r+s-2p) \right] \bar{\boldsymbol{\varepsilon}}_1 + \frac{r-p}{q-p} \bar{\boldsymbol{\varepsilon}}_2 + \frac{s-p}{q-p} \bar{\boldsymbol{\varepsilon}}_3, \quad (3.12)$$

where $p = \frac{1}{6}$ and $q = \frac{4}{6}$ are constant values that indicate the locations of the integration points [31].

The deviatoric strain of 3-node strain-smoothed element is also defined from the smoothed strains allocated at integration points, as in Eq. 3.12, and forms a linear field within the element, as follows:

$${}^{dev}\bar{\boldsymbol{\epsilon}}(r,s) = \left[1 - \frac{1}{q-p}(r+s-2p) \right] {}^{dev}\bar{\boldsymbol{\epsilon}}_1 + \frac{r-p}{q-p} {}^{dev}\bar{\boldsymbol{\epsilon}}_2 + \frac{s-p}{q-p} {}^{dev}\bar{\boldsymbol{\epsilon}}_3. \quad (3.13)$$

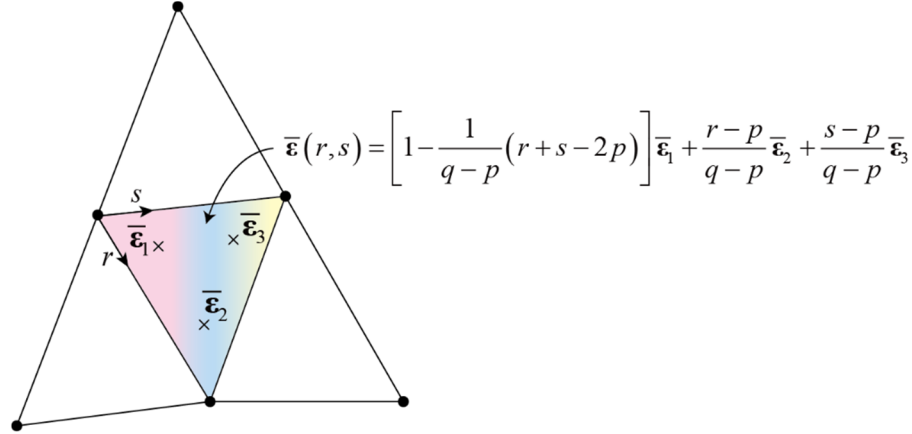


Fig. 3.5. The linear strain field within a 3-node triangular element through SSE method.

3.2.2 Smoothed volumetric strain by strain-smoothed element method

To alleviate the volumetric locking, a new volumetric strain is defined using the previously calculated smoothed strains. A nodal smoothed strain value is obtained using the smoothed strains at the integration points near the node, as shown colored nodes and its neighboring integration points in **Fig. 3.6**.

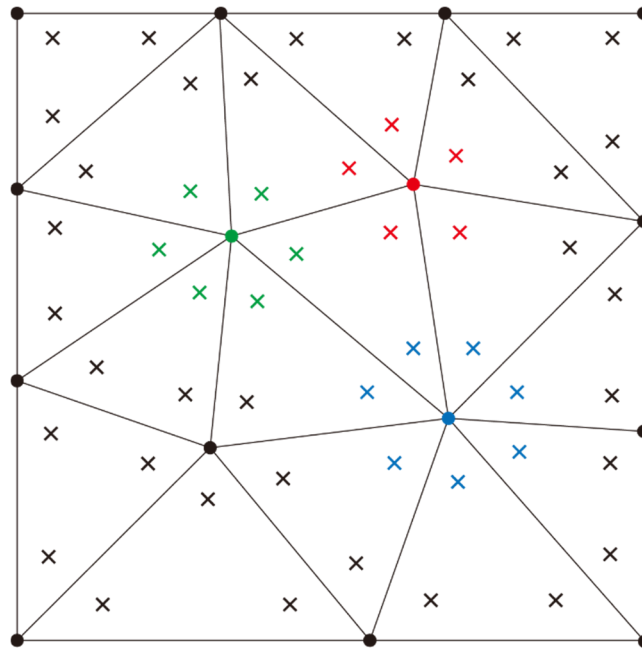


Fig. 3.6. A node and its neighboring integration points in a triangular mesh.

The volumetric strain at the node i , i.e., $({}^{vol}\bar{\varepsilon})_{node\ i}$ is defined using the strains at the integration points near the node i from n neighboring element as follows:

$$({}^{vol}\bar{\varepsilon})_{node\ i} = \frac{\sum_{k=1}^n {}^{vol}\bar{\varepsilon}_k A_k}{\sum_{k=1}^n A_k}, \quad (3.14)$$

where A_k is area of neighboring element k , and ${}^{vol}\bar{\varepsilon}_k$ is the smoothed strain at the integration point near the node i in neighboring element k , as shown in **Fig. 3.7**.

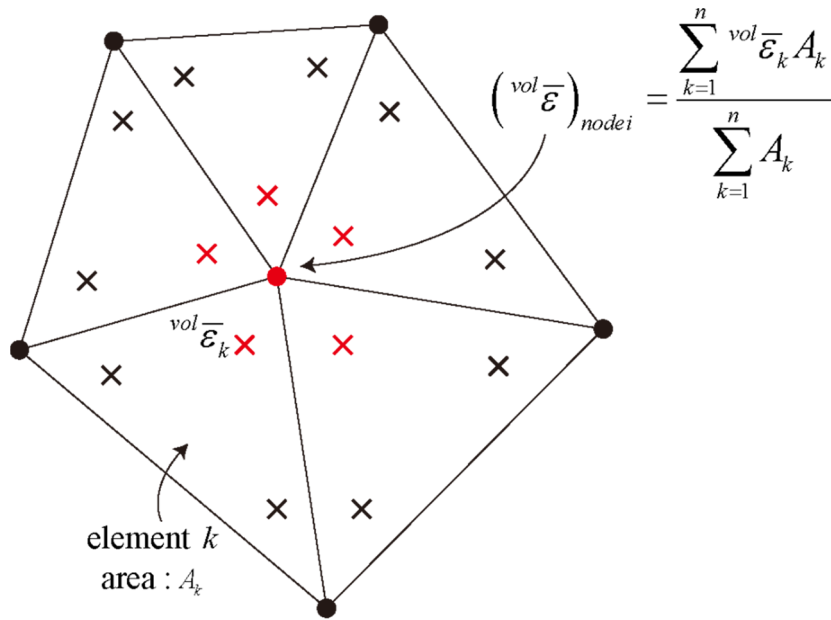


Fig. 3.7. The nodal smoothed volumetric strain obtained from the neighboring smoothed strains.

The strain field within an element is defined from the smoothed volumetric strains at the nodes. As shown in **Fig. 3.8**, the strain field is obtained using the shape functions of the standard isoparametric procedure for the 3-node triangular domain as follows:

$${}^{vol}\bar{\varepsilon}(r, s) = \sum_{k=1}^3 h_k ({}^{vol}\bar{\varepsilon})_i \quad \text{with } h_1 = r, \quad h_2 = s, \quad h_3 = 1 - r - s. \quad (3.15)$$

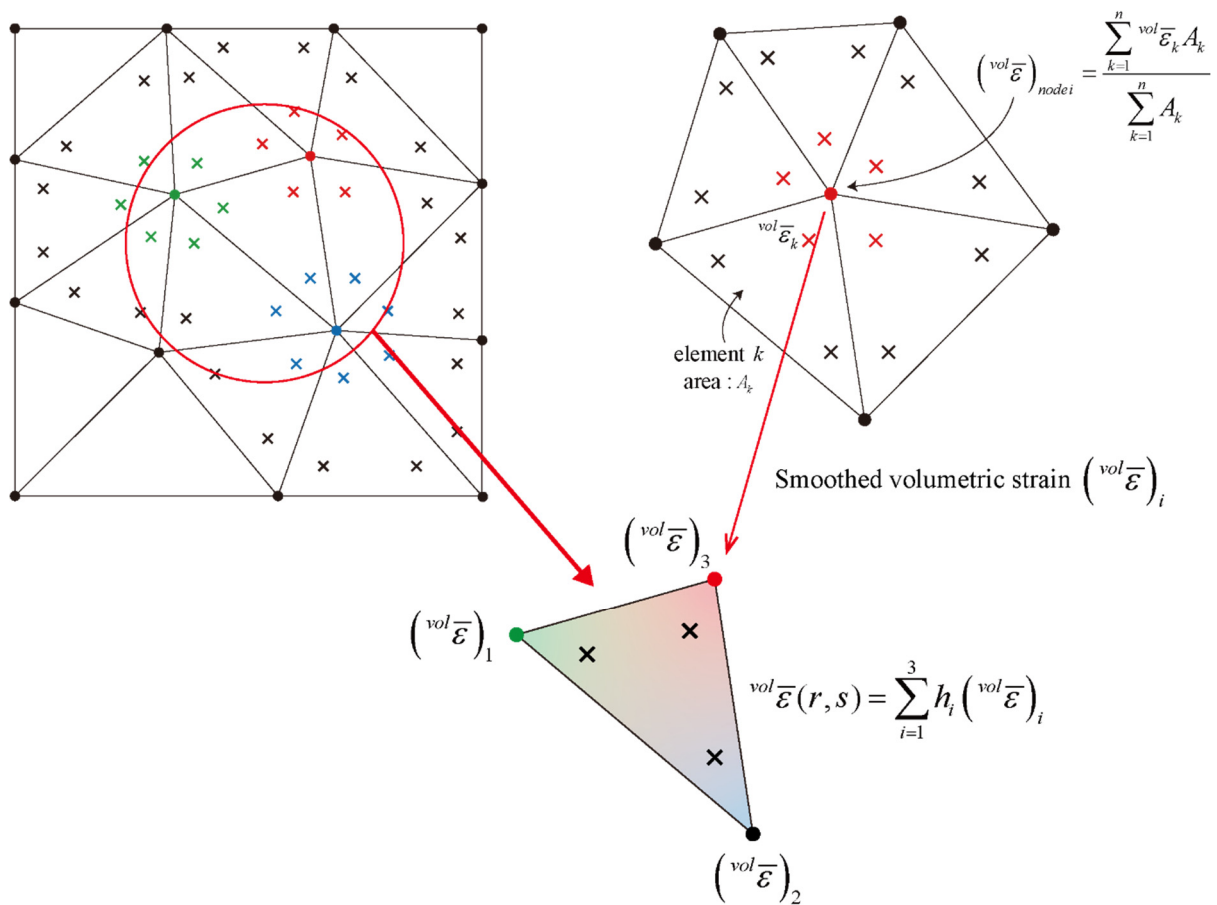


Fig. 3.8. Nodal smoothed volumetric strains and a volumetric strain field within an element.

The strain being defined based on the node is similar to the node-based smoothed finite element (NS-FEM). However, the smoothed strains for NS-FEM are determined according to the smoothing domains, whereas the proposed method defines smoothed strains at nodes using the strain calculated through the SSE method and the strain field is formed within an element, see **Fig. 3.9**.

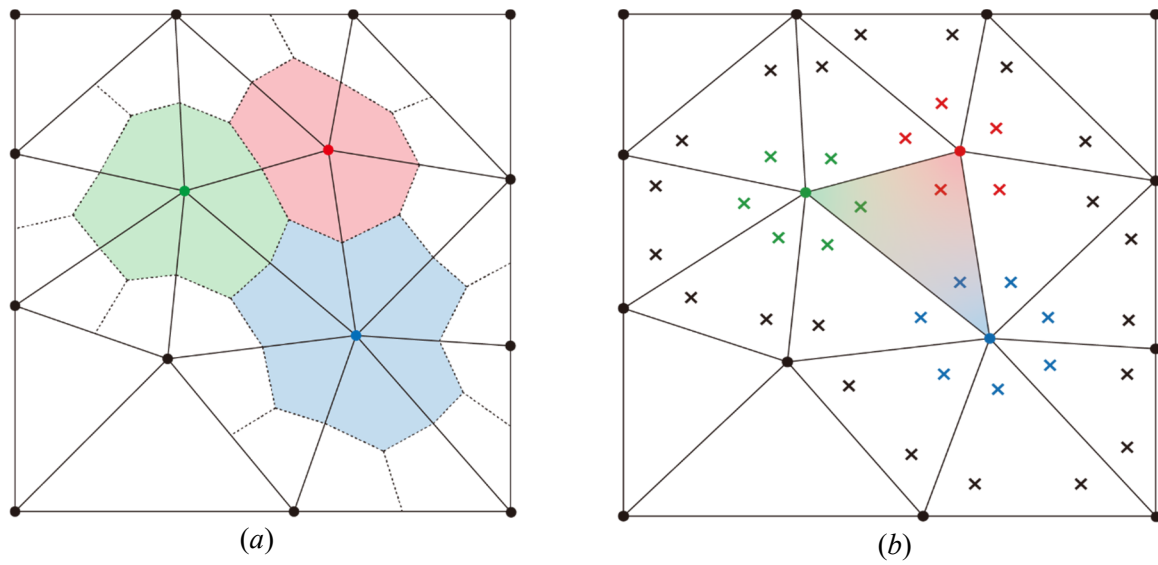


Fig. 3.9. (a) Smoothing domains for the node-based smoothed finite element. (b) A strain field within an element for the strain-smoothed element.

3.3 Basic numerical tests

We conduct basic numerical tests on the strain-smoothed 3-node triangular element with alleviated volumetric locking, including tests for isotropic element, zero-energy modes, and patch tests [1].

The suggested elements produce consistent results regardless of the node numbering sequences, demonstrating their success in passing the isotropic element test.

If no constraint exists on a single 2D solid element, then the stiffness matrix of the element must contain only three zero-energy modes corresponding to the rigid body modes. The zero-energy mode tests are performed using the single triangular element, and the proposed elements pass the zero-energy mode tests.

For the patch tests, the minimum number of DOFs is constrained to prevent rigid body motions, and appropriate loadings are applied to obtain a constant stress field. The same stress value should be obtained at all points on the elements to pass the patch tests. The mesh shown in **Fig. 3.10** is used to perform the normal and shear stress patch tests, and the boundary conditions to obtain the constant stress field are depicted in **Fig. 3.11**. The stress values are obtained from all Gauss integration points. The relative errors in the stress obtained from the proposed triangular element are on the order of 10^{-14} to 10^{-15} . These are similar to numerical errors that occur in computations with 16 significant digits. Therefore, the proposed element successfully passes the test with acceptable accuracy.

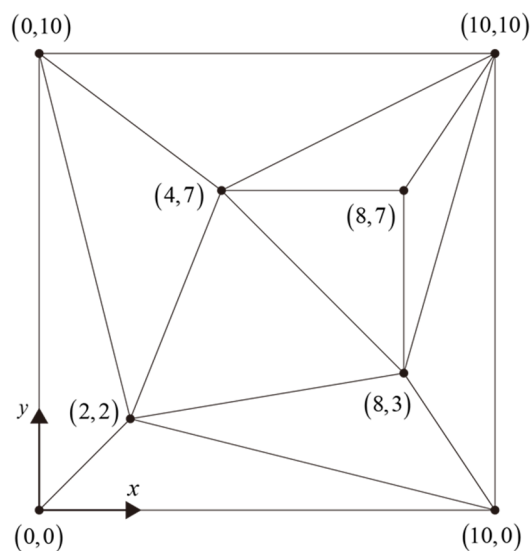


Fig. 3.10. A 2D triangular finite mesh used for the patch test.

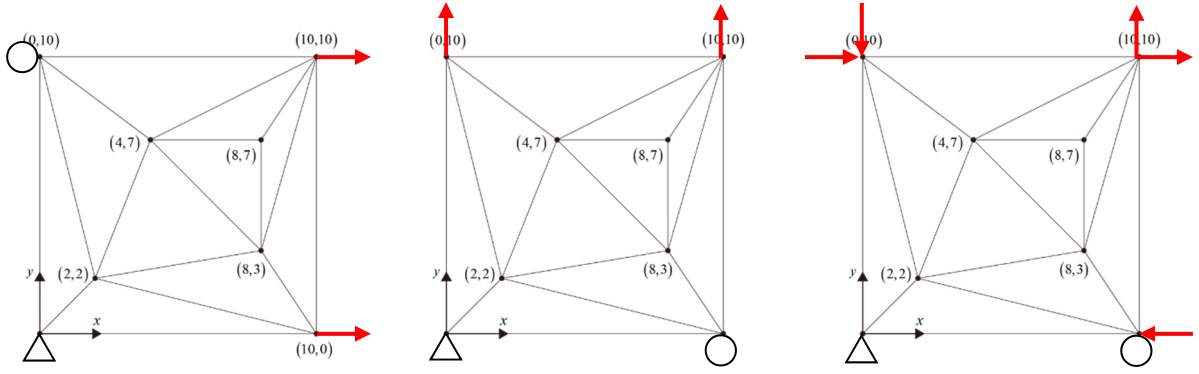


Fig. 3.11. The uniform stress conditions for the patch test.

3.4 Numerical examples

We investigate the performance of the strain-smoothed 3-node triangular finite element by solving the four numerical examples: a square block problem, an infinite plate with a circular hole, Cook's skew beam, and a dam problem. The unit thickness is considered for all the 2D solid problems.

The performance of the proposed strain-smoothed 3-node triangular finite element with treatment of volumetric locking is compared with the edge-based smoothed finite elements (ES-FEM) [28] and the node-based smoothed finite elements (NS-FEM) for 3-node triangular elements. Additionally, the performance of the proposed element is compared with the strain-smoothed finite element that has no treatment for volumetric locking (SSE). The accuracy of elements and the alleviation of volumetric locking is assessed using convergence curves.

Reference solutions are obtained using sufficiently fine meshes of 9-node quadrilateral finite elements with selective reduced integration for the volumetric term.

To measure the convergence of the finite elements, the s-norm proposed by Hiller and Bathe is measured, and it is defined as follows [46]:

$$\|\mathbf{u}_{ref} - \mathbf{u}_h\|_S^2 = \int_{\Omega_{ref}} \Delta \boldsymbol{\varepsilon}^T \Delta \boldsymbol{\tau} d\Omega_{ref} \quad \text{with} \quad \Delta \boldsymbol{\varepsilon} = \boldsymbol{\varepsilon}_{ref} - \boldsymbol{\varepsilon}_h, \quad \Delta \boldsymbol{\tau} = \boldsymbol{\tau}_{ref} - \boldsymbol{\tau}_h, \quad (3.16)$$

where \mathbf{u}_{ref} is the reference solution, \mathbf{u}_h is the solution of the finite element discretization, and $\boldsymbol{\varepsilon}$ and $\boldsymbol{\tau}$ are the strain and stress vectors, respectively.

To observe the convergence behavior, the normalized relative error E_h is measured as follows:

$$E_h = \frac{\|\mathbf{u}_{ref} - \mathbf{u}_h\|_S^2}{\|\mathbf{u}_{ref}\|_S^2}. \quad (3.17)$$

The optimal convergence behavior for linear elements is expressed as

$$E_r \cong ch^2, \quad (3.18)$$

where c is a constant and h is the element size [1].

3.4.1 Square block problem

A 2D square block is subjected to a compression pressure of total magnitude $P=1$ at the right half top of the structure, and the bottom of the structure is clamped as shown in **Fig. 3.12(a)**. The plane strain condition is assumed with Young's modulus $E = 3 \times 10^7$. Poisson's ratio is considered for the values $\nu = 0.3, 0.49, 0.499$ and 0.4999 .

The regular and distorted meshes of $N \times N$ elements with $N = 4, 8, 16$ and 32 are used to obtain the solutions, and the mesh examples for $N = 4$ is shown in **Fig. 3.12(b)** and (c). To create the distorted meshes, the nodes within the elements are shifted according to the following rule [33]:

$$x' = x - \alpha h_x, \quad (3.19)$$

$$y' = y - \beta \gamma h_y, \quad (3.20)$$

where (x, y) and (x', y') are the position vector of nodes in the regular and distorted meshes, respectively, h_x and h_y are the size of elements in x and y directions for the regular meshes, the constants are applied as $\alpha = 0.3$, $\beta = 0.4$, and γ is defined to a random real number between -1 and 1 . The distorted meshes formed through the previously mentioned process are as shown in **Fig. 3.13**.

The convergence curves for E_r in Eq. (3.17) with regular meshes and distorted meshes are shown in **Fig. 3.14** and **Fig. 3.15**, respectively. The reference solutions are obtained using a 128×128 mesh of 9-node quadrilateral elements with selective reduced integration for the volumetric term. When the Poisson's ratio is 0.3 , the SSE demonstrates significantly better convergence behaviors compared to other elements. However, in cases where volumetric locking may occur, noticeable performance degradation is observed, and this is also the case for the ES-FEM. On the other side, NS-FEM exhibits slightly lower performance but is relatively free from volumetric locking, and it shows better convergence performance in cases where volumetric locking may occur due to the Poisson's ratio. The proposed element demonstrates improved performance even in situations where volumetric locking does not occur. Additionally, as the Poisson's ratio approaches 0.5 , improved convergence behavior is observed as volumetric locking is significantly alleviated.

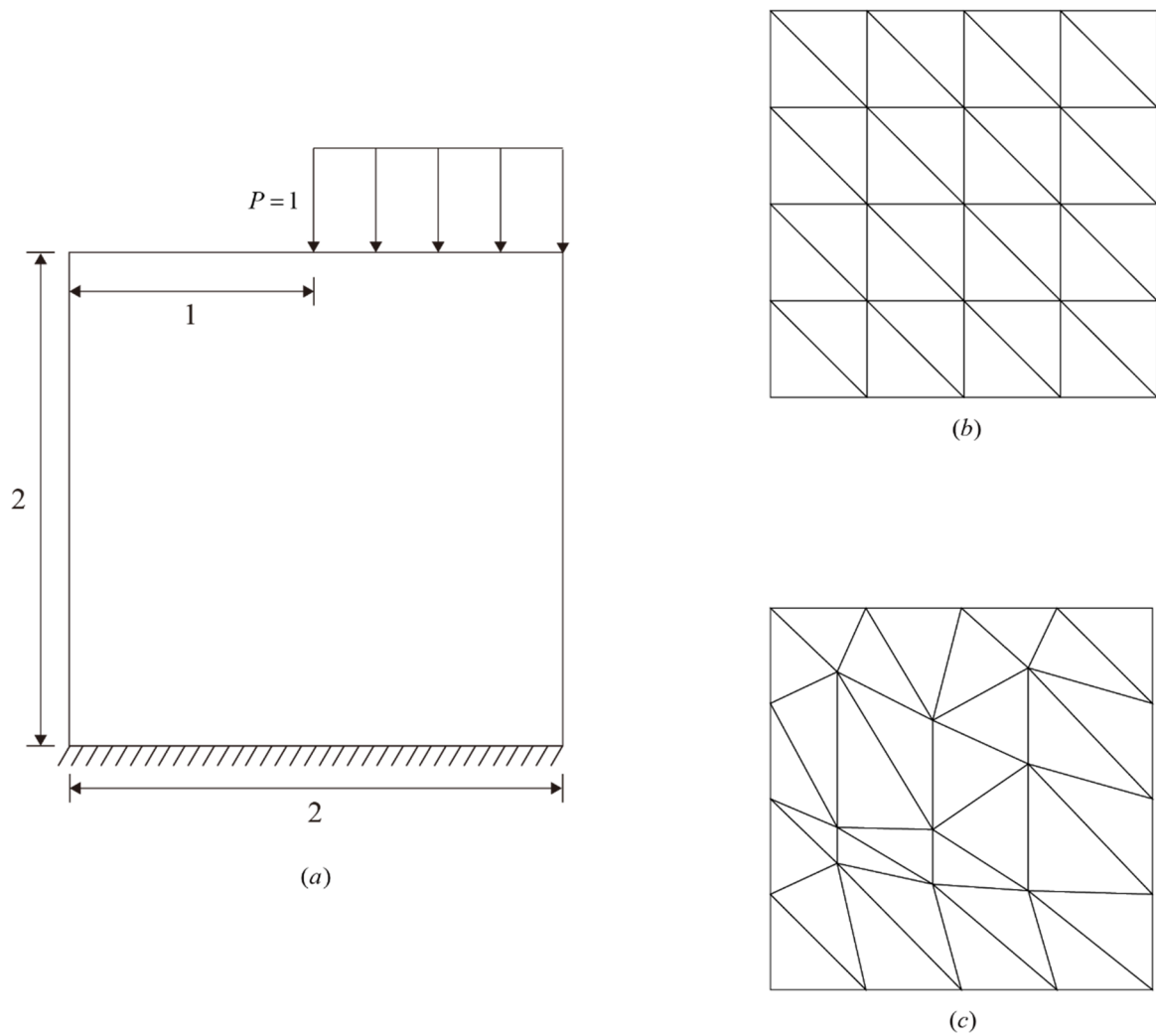


Fig. 3.12. (a) The square block problem ($E = 3 \times 10^7$ and $\nu = 0.3, 0.49, 0.499$ and 0.4999). (b) A regular mesh and (c) a distorted mesh at $N = 4$ used for the square block problem.

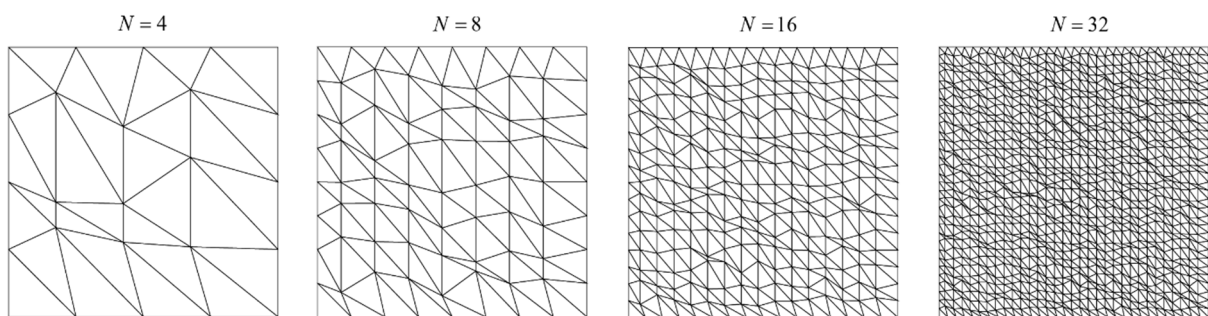


Fig. 3.13. Distorted meshes used for the square block problem.

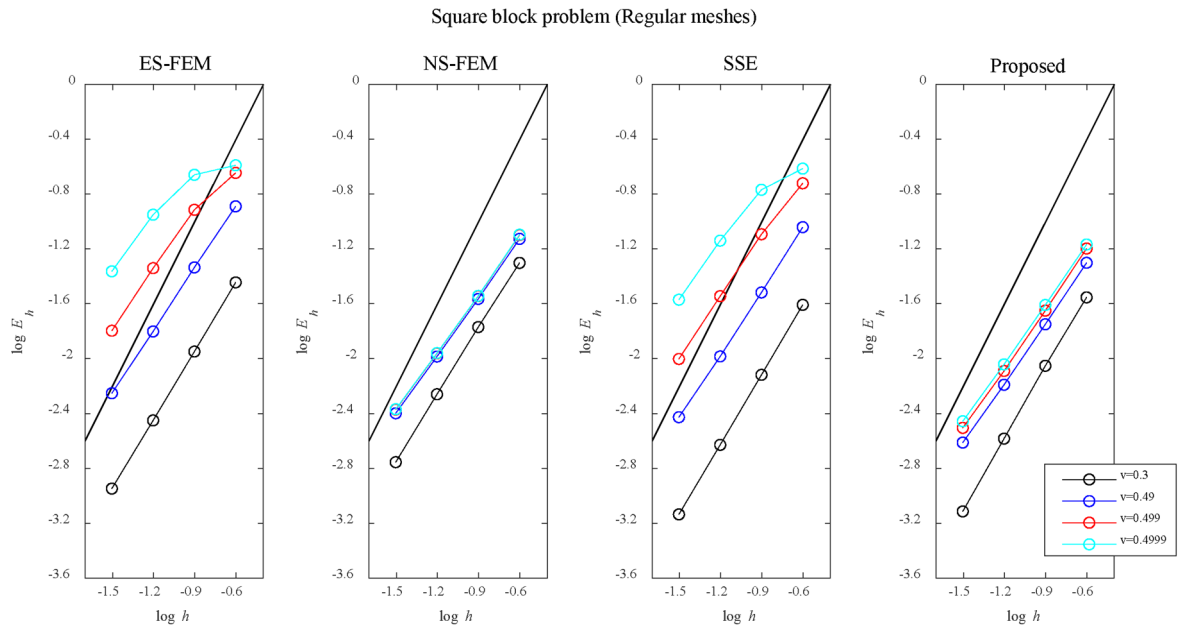


Fig. 3.14. Convergence curves for the square block problem with regular meshes. The bold line represents the optimal convergence rate.

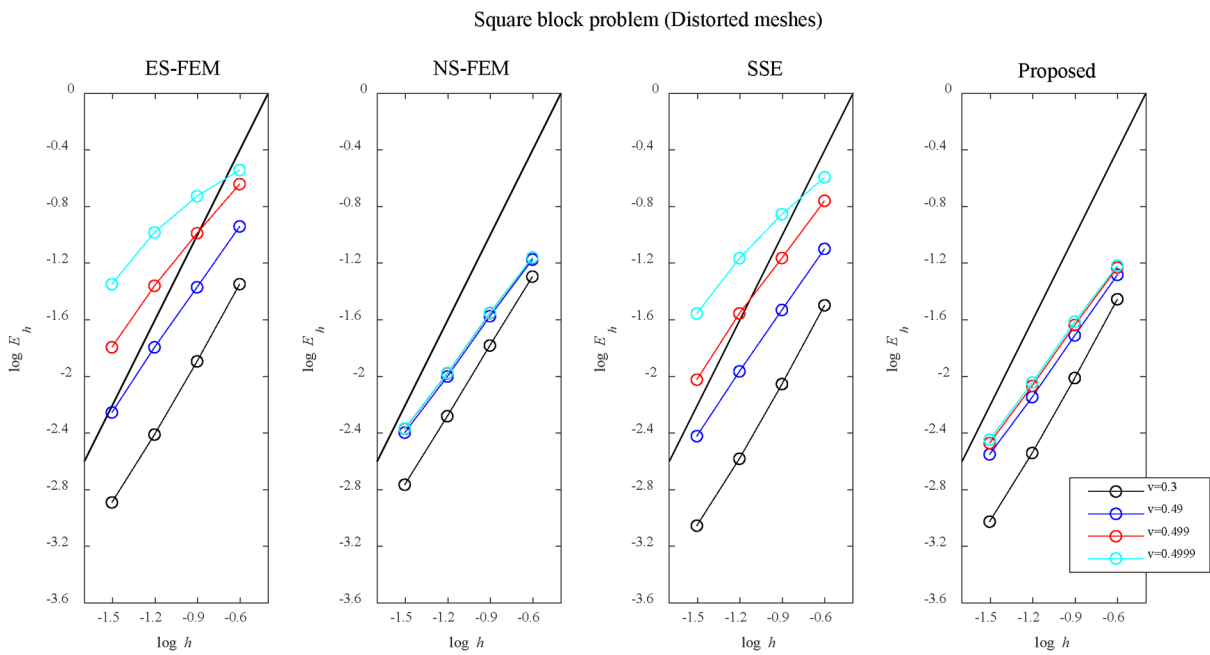


Fig. 3.15. Convergence curves for the square block problem with distorted meshes. The bold line represents the optimal convergence rate.

3.4.2 Infinite plate with a circular hole

We solve the problem of infinite plate with a circular hole shown in **Fig. 3.16(a)** [22,31]. The radius of the circular hole is $a = 1$, and the infinite plate is subjected to a far-field traction $p = 1$ in the x -direction. The plane strain condition is considered with Young's modulus $E = 3 \times 10^7$ and several Poisson's ratio $\nu = 0.3, 0.49, 0.499$ and 0.4999 . Due to symmetry, a quarter of the plate is modeled as shown in **Fig. 3.16(a)**, and the corresponding boundary conditions are imposed as follows: $u = 0$ along BC and $v = 0$ along AE . The model is comprised of two sets of $N \times N$ elements meshes (with $N = 4, 8, 16$ and 32) that are symmetric about the diagonal, and the mesh example for $N = 8$ is shown in **Fig. 3.16(b)**.

The traction boundary conditions are imposed along CD and DE using the following analytical solutions [35]:

$$\sigma_{xx}(r, \theta) = p \left(1 - \frac{a^2}{r^2} \left(\frac{3}{2} \cos 2\theta + \cos 4\theta \right) + \frac{3a^4}{2r^4} \cos 4\theta \right), \quad (3.21)$$

$$\sigma_{yy}(r, \theta) = p \left(-\frac{a^2}{r^2} \left(\frac{1}{2} \cos 2\theta - \cos 4\theta \right) - \frac{3a^4}{2r^4} \cos 4\theta \right), \quad (3.22)$$

$$\sigma_{xy}(r, \theta) = p \left(-\frac{a^2}{r^2} \left(\frac{1}{2} \sin 2\theta + \sin 4\theta \right) + \frac{3a^4}{2r^4} \sin 4\theta \right), \quad (3.23)$$

where r and θ are the distance from the origin ($x = y = 0$) and counterclockwise angle from the positive x -axis, respectively.

The convergence curves obtained using E_r in Eq. (3.17) are shown in **Fig. 3.17**. The reference solutions are obtained using a mesh with $N = 128$ of 9-node quadrilateral elements with selective reduced integration for the volumetric term. When the Poisson's ratio is 0.3, the proposed element exhibits convergence performance comparable to SSE, and even when the Poisson's ratio approaches 0.5, it demonstrates convergence behavior with relatively alleviated volumetric locking.

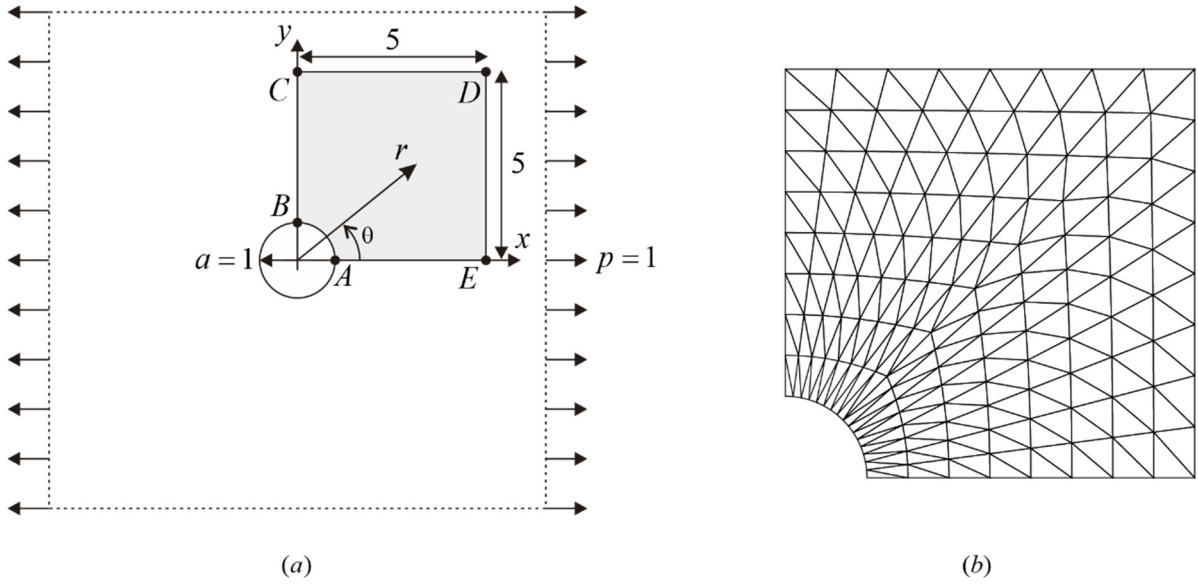


Fig. 3.16. (a) Infinite plate with a circular hole ($E = 3 \times 10^7$ and $\nu = 0.3, 0.49, 0.499$ and 0.4999). (b) A mesh at $N = 8$ used for the problem.

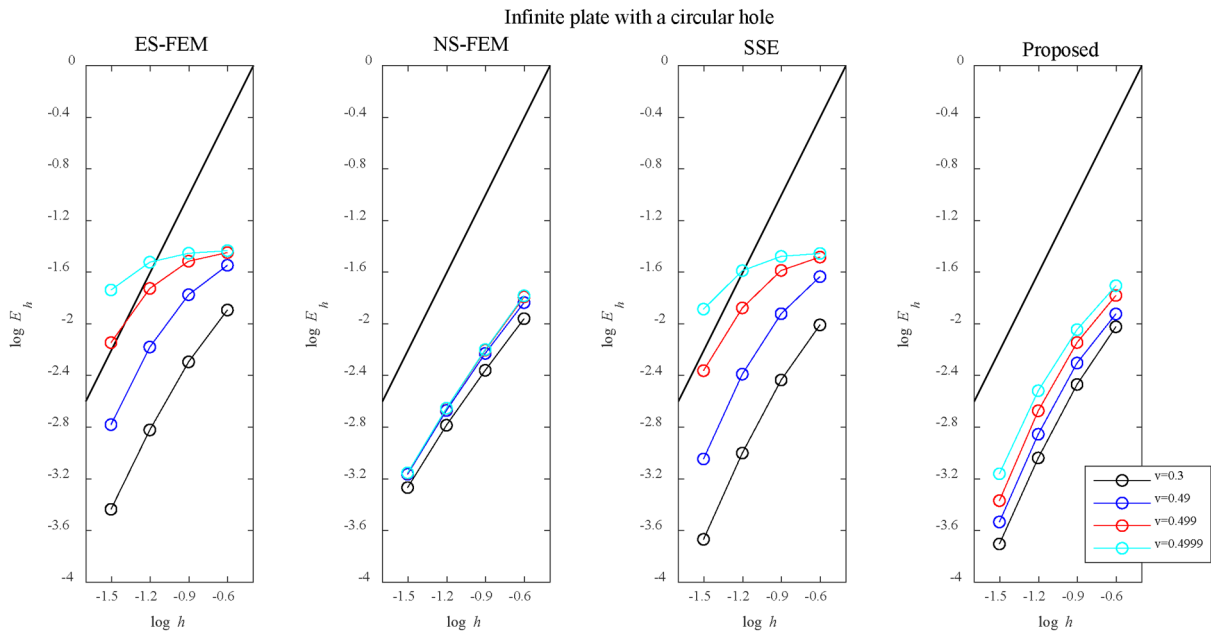
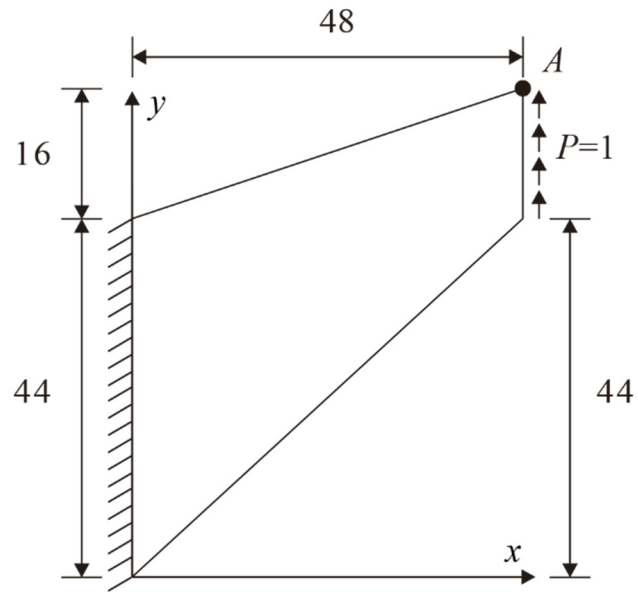


Fig. 3.17. Convergence curves for the problem of infinite plate with a circular hole. The bold line represents the optimal convergence rate.

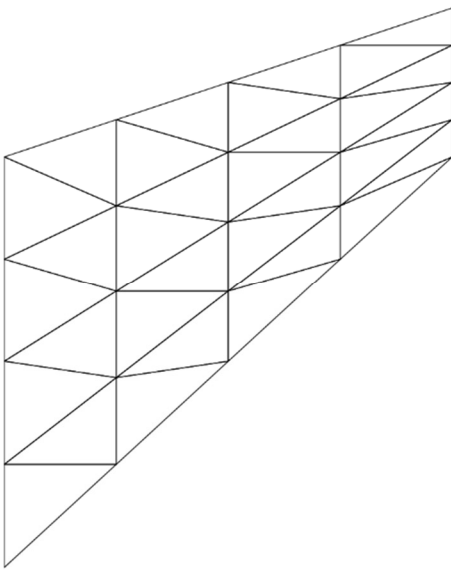
3.4.3 Cook's skew beam

To the next, the Cook's skew beam problem is considered, as shown in **Fig. 3.18** [3]. The left side of the structure is clamped, and a distributed shearing force of total magnitude $P=1$ is exerted on the right edge. The plane strain condition is assumed with Young's modulus $E=3\times 10^7$ and Poisson's ratio is considered for the values $\nu=0.3, 0.49, 0.499$ and 0.4999 . Solutions are obtained for the regular and distorted meshes of $N\times N$ elements with $N=4, 8, 16$ and 32 , and the mesh examples for $N=4$ is shown in **Fig. 3.18**(b) and (c). To create the distorted meshes, node remapping process is performed as Eq. (3.19) and (3.20). The distorted meshes example formed through the process are as shown in **Fig. 3.19**.

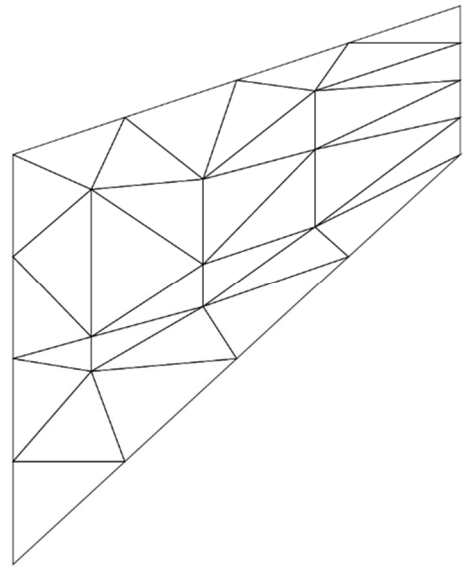
The convergence curves for E_r in Eq. (3.17) with regular meshes and distorted meshes are shown in **Fig. 3.20** and **Fig. 3.21**, respectively. The reference solutions are obtained using a 128×128 mesh of 9-node quadrilateral elements with selective reduced integration for the volumetric term. As evident from the convergence curves as **Fig. 3.20** and **3.21**, NS-FEM exhibits convergence performance that is free from volumetric locking, but it has slightly lower convergence accuracy overall. Furthermore, ES-FEM and SSE show excellent performance in the cases not related to volumetric locking. However, their performance deteriorates as the Poisson's ratio approaches 0.5. The proposed element provides improved convergence performance at Poisson's ratios far from volumetric locking and maintains its performance even in situations where volumetric locking may occur.



(a)



(b)



(c)

Fig. 3.18. (a) The Cook's skew beam problem ($E = 3 \times 10^7$ and $\nu = 0.3, 0.49, 0.499$ and 0.4999). (b) A regular mesh and (c) a distorted mesh at $N = 4$ used for the cook's beam problem.

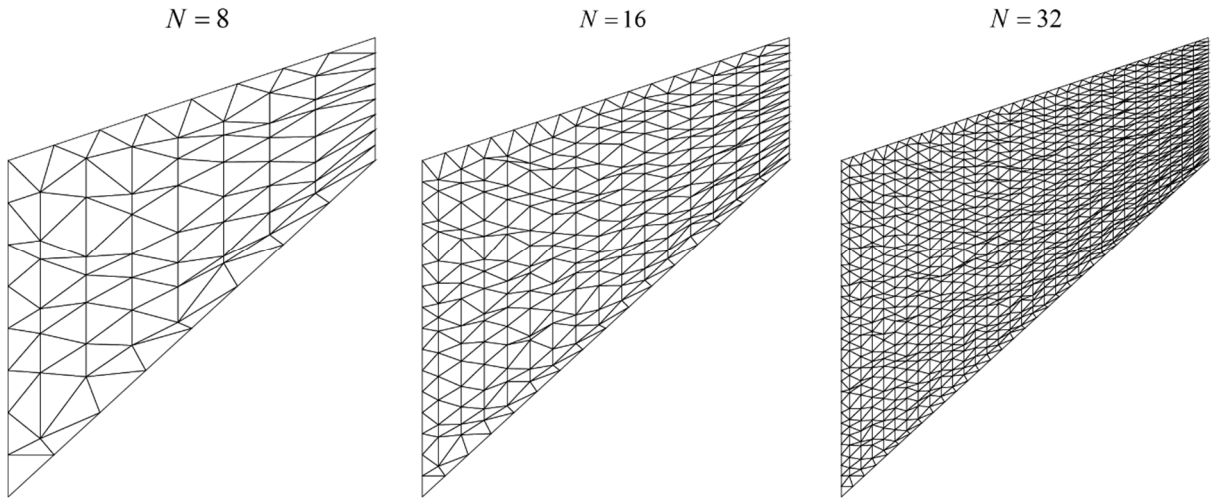


Fig. 3.19. Examples of distorted meshes used for the Cook's skew beam problem.

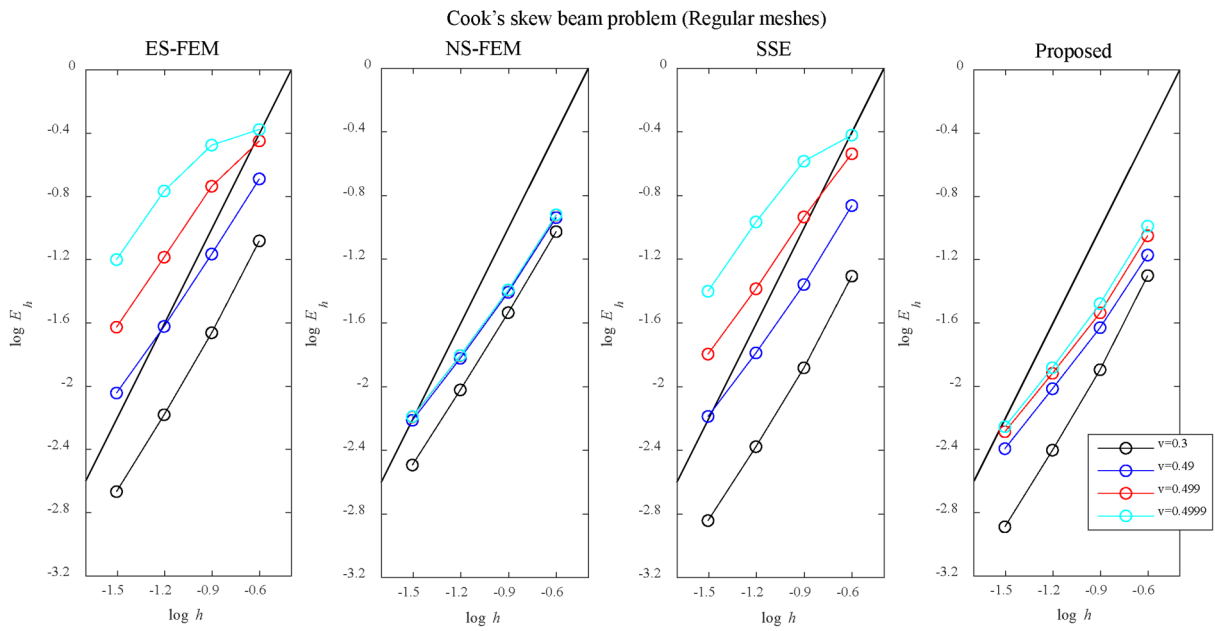


Fig. 3.20. Convergence curves for the Cook's skew beam problem with regular meshes. The bold line represents the optimal convergence rate.

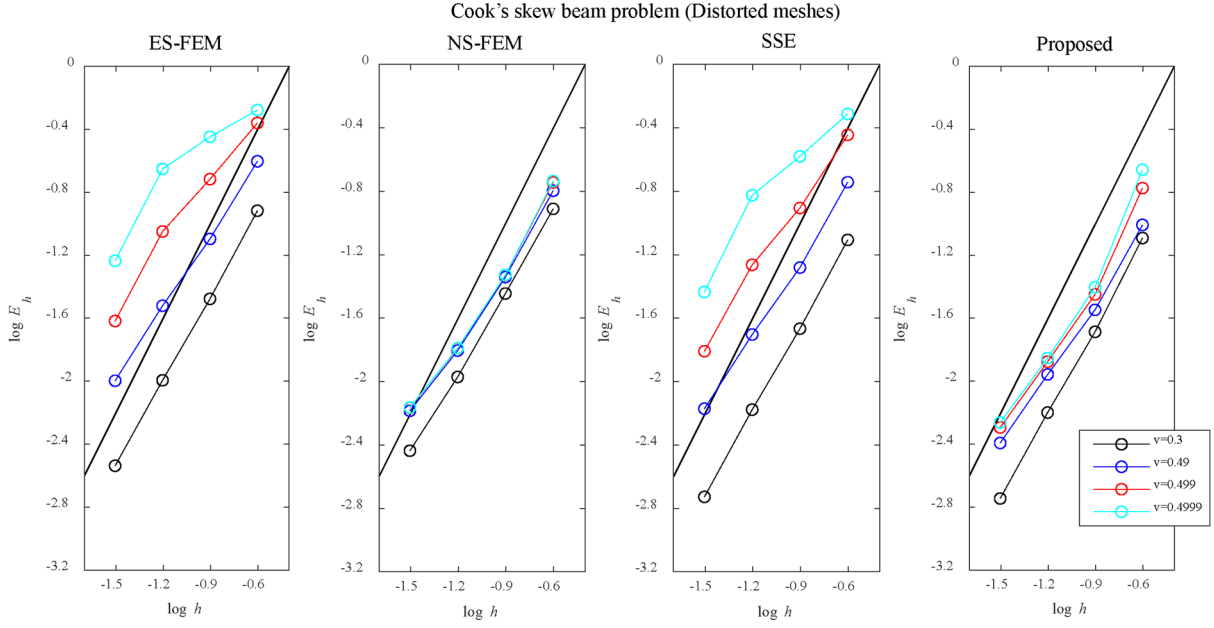


Fig. 3.21. Convergence curves for the Cook's skew beam problem with distorted meshes. The bold line represents the optimal convergence rate.

3.4.4 Dam problem

A 2D dam structure is applied to the surface force described below on its left edge, as shown in **Fig. 3.22(a)**:

$$f_s = \begin{cases} 5-y & 0 \leq y \leq 5 \\ (y-5)^{1/5} & 5 \leq y \leq 10 \end{cases} . \quad (3.24)$$

The bottom of the dam structure is clamped, and the plane strain condition is employed with Young's modulus $E = 3 \times 10^{10}$, and various Poisson's ratios such as $\nu = 0.3, 0.49, 0.499$ and 0.4999 are considered. The meshes with $N \times 2N$ elements are used to obtain the solution, where $N = 4, 8, 16$ and 32 , and **Fig. 3.22(b)** is example of mesh at $N = 4$.

The convergence curves are obtained using E_r in Eq. (3.17), as shown in **Fig. 3.23**. The reference solutions are obtained using a 128×256 mesh of 9-node quadrilateral elements with selective reduced integration for the volumetric term. In the case of the Poisson's ratio of 0.3 , it is observed that the SSE, without any volumetric locking treatment, demonstrates excellent convergence performance. The proposed element also demonstrates improved convergence performance nearly similar to SSE in situations where locking does not occur. However, as the Poisson's ratio approaches 0.5 , the performance of SSE deteriorates significantly. The performance of SSE

is even worse than that of NS-FEM, which is not particularly notable in terms of performance compared to other elements. The proposed element exhibits improved convergence behavior with significant alleviation of volumetric locking, even within the range where the Poisson's ratio could induce volumetric locking.

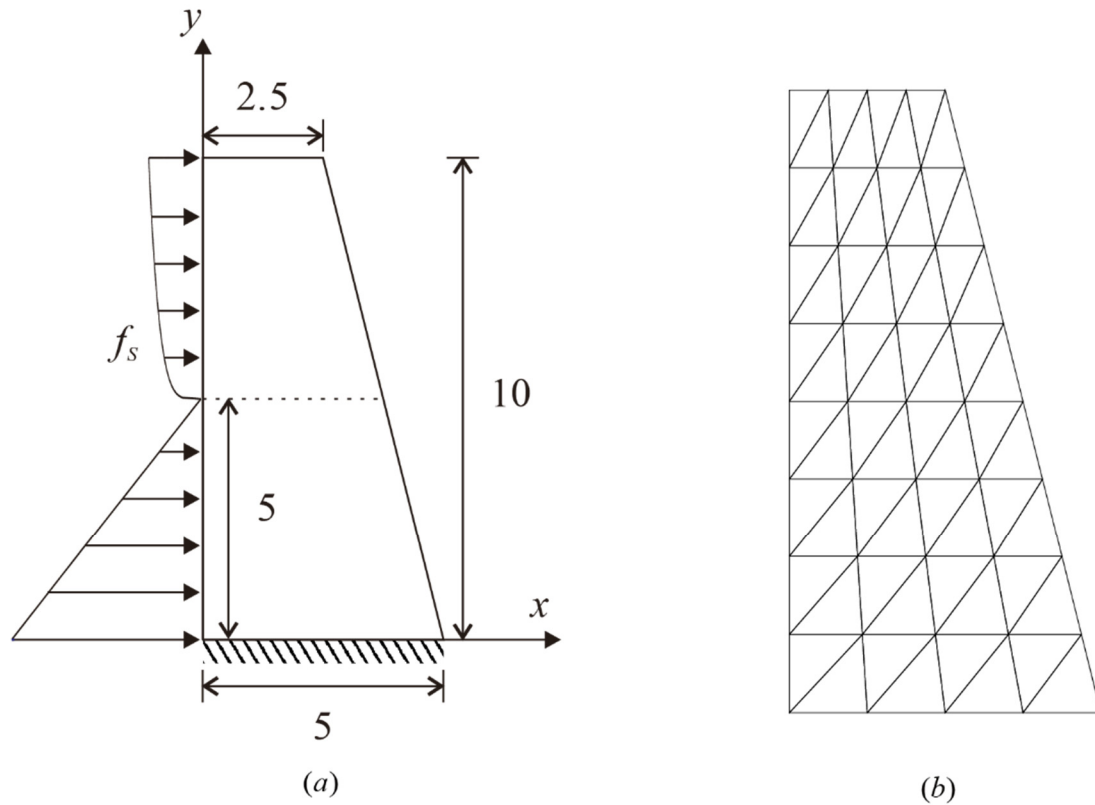


Fig. 3.22. (a) Dam problem ($E = 3 \times 10^{10}$ and $\nu = 0.3, 0.49, 0.499$ and 0.4999). (b) A mesh at $N = 4$ used for the dam problem.

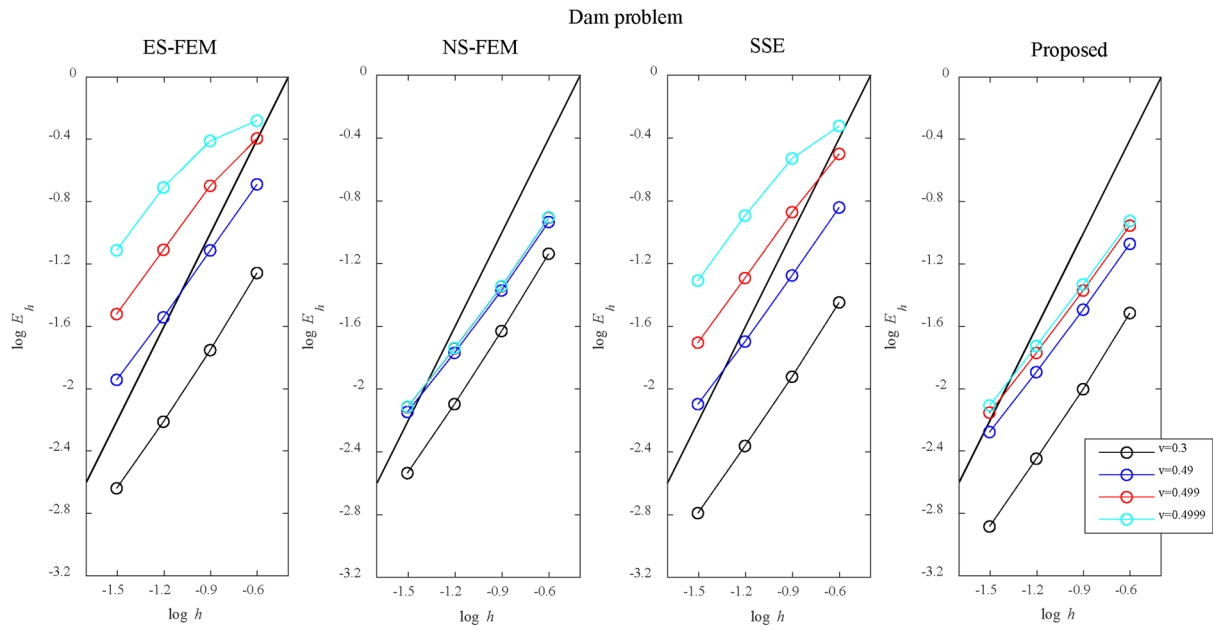


Fig. 3.23. Convergence curves for the dam problem. The bold line represents the optimal convergence rate.

Chapter 4. Concluding Remark

In this study, we proposed the strain-smoothed polygonal finite elements. Instead of using complex shape functions for polygonal elements, piecewise linear shape functions were employed to triangulate the elements for strain smoothing. We first calculated the smoothed strains for the elements using all the strains of all neighboring elements. Subsequently, smoothed strains were assigned to the vertices of the sub-triangles of the elements, which resulted in a piecewise linear strain field for the strain-smoothed polygonal elements.

The strain-smoothed polygonal elements passed the basic tests (i.e., isotropic element, zero-energy mode, and patch tests). In addition, the elements showed improved convergence behaviors compared with previously developed elements in various numerical examples. The strain-smoothed polygonal elements can be effectively used in various applications, such as contact problems on non-conformal meshes [6,11] and crack analysis with minimal remeshing [8,12].

In addition, we proposed the strain-smoothed 3-node triangular finite element with volumetric locking alleviation. While the strain-smoothed 3-node triangular finite element has a linear strain field within the element, there is an issue where assuming constant volumetric strain does not alleviate volumetric locking. To address volumetric locking, the smoothed strains are separated into their volumetric and deviatoric strains. Similar to the general integration process, the deviatoric strain field within the element is formed from the deviatoric strains at the integration points. The volumetric strains are utilized to define the newly smoothed volumetric strains on a node-wise basis. A nodal smoothed volumetric strain is obtained using the smoothed volumetric strains at integration points near the node. Based on the smoothed volumetric strains at the nodes, the volumetric strain field within the element is established.

The performance of the proposed strain-smoothed 3-node triangular finite element is compared with various smoothed elements such as the edge-based smoothed finite elements (ES-FEM), the node-based smoothed finite elements (NS-FEM), and the strain-smoothed finite element that has no treatment for volumetric locking (SSE). In the cases where volumetric locking does not occur, SSE demonstrates excellent performance. However, as the Poisson's ratio approaches 0.5, its performance deteriorates significantly. On the other hand, NS-FEM, while being a volumetric-locking-free smoothing element, exhibits somewhat lower convergence performance regardless of the Poisson's ratio. The proposed element provides improved convergence performance in situations far from volumetric locking, and it sustains its performance even in situations where volumetric locking may occur. The strain-smoothed triangular element with alleviated volumetric locking can be utilized for the analysis of materials that are nearly incompressible, such as rubber [40].

Bibliography

- [1] Bathe KJ (1996) Finite element procedures, 2nd ed. Prentice Hall, Bathe KJ (2014) Watertown, MA, and Higher Education Press (2016) China
- [2] Hughes TJR (2000) The finite element method: Linear static and dynamic finite element analysis. Dover Publications, Mineola, NY
- [3] Cook RD (2007) Concepts and applications of finite element analysis. John Wiley & Sons, New York
- [4] Tabarraei A, Sukumar N (2006) Application of polygonal finite elements in linear elasticity. *Int J Comput Methods* 03:503–20
- [5] Biabanaki SOR, Khoei AR (2012) A polygonal finite element method for modeling arbitrary interfaces in large deformation problems. *Comput Mech* 50:19–33
- [6] Biabanaki SOR, Khoei AR, Wriggers P (2014) Polygonal finite element methods for contact-impact problems on non-conformal meshes. *Comput Methods Appl Mech Eng* 269:198–221
- [7] Ho-Nguyen-Tan T, Kim HG (2018) A new strategy for finite-element analysis of shell structures using trimmed quadrilateral shell meshes: A paving and cutting algorithm and a pentagonal shell element. *Int J Numer Methods Eng* 114:1–27
- [8] Khoei AR, Yasbolaghi R, Biabanaki SOR (2015) A polygonal finite element method for modeling crack propagation with minimum remeshing. *Int J Fract* 194:123–48
- [9] Talischi C, Paulino GH, Pereira A, Menezes IFM (2012) PolyMesher: A general-purpose mesh generator for polygonal elements written in MATLAB. *Struct Multidiscip Optim* 45:309–28
- [10] Yan DM, Wang W, Lévy B, Liu Y (2013) Efficient computation of clipped Voronoi diagram for mesh generation. *CAD Comput Aid Des* 45:843–52
- [11] Khoei AR, Yasbolaghi R, Biabanaki SOR (2015) A polygonal-FEM technique in modeling large sliding contact on non-conformal meshes: A study on polygonal shape functions. *Eng Comput (Swansea W)* 32:1391–431
- [12] Nguyen NV, Lee D, Nguyen-Xuan H, Lee J (2020) A polygonal finite element approach for fatigue crack growth analysis of interfacial cracks. *Theor Appl Fract Mech* 108:102576
- [13] Huang X, Ding W, Zhu Y, Yang C (2017) Crack propagation simulation of polycrystalline cubic boron nitride abrasive materials based on cohesive element method. *Comput Mater Sci* 138:302–14
- [14] Wachspress EL (1975) A rational finite element basis. *Math Sci Eng*. NY: Academic Press 114
- [15] Floater MS (2003) Mean value coordinates. *Comput Aid Geom Des* 20:19–27
- [16] Sukumar N, Tabarraei A (2004) Conforming polygonal finite elements. *Int J Numer Methods Eng* 61:2045–66
- [17] Thomes RL, Menandro FCM (2020) Polygonal finite element: A comparison of the stiffness matrix integration methods. *Appl Math Comput* 375:125089
- [18] Natarajan S, Bordas S, Roy Mahapatra D (2009) Numerical integration over arbitrary polygonal domains based on Schwarz–Christoffel conformal mapping. *Int J Numer Methods Eng* 80:103–34
- [19] Talischi C, Pereira A, Paulino GH, Menezes IFM, Carvalho MS (2014) Polygonal finite elements for

- incompressible fluid flow. *Int J Numer Meth Fluids* 74:134–51
- [20] Nguyen-Xuan H (2017) A polygonal finite element method for plate analysis. *Comput Struct* 188:45–62
- [21] Chen JS, Wu CT, Yoon S, You Y (2001) Stabilized conforming nodal integration for Galerkin mesh-free methods. *Int J Numer Methods Eng* 50:435–66.
- [22] Liu GR, Dai KY, Nguyen TT (2007) A smoothed finite element method for mechanics problems. *Comput Mech* 39:859–77
- [23] Dai KY, Liu GR, Nguyen TT (2007) An n-sided polygonal smoothed finite element method (nSFEM) for solid mechanics. *Finite Elem Anal Des* 43:847–60
- [24] Nguyen-Thanh N, Rabczuk T, Nguyen-Xuan H, Bordas SPA (2008) A smoothed finite element method for shell analysis. *Comput Methods Appl Mech Eng* 198:165–77
- [25] Liu GR, Nguyen-Thoi T, Nguyen-Xuan H, Lam KY (2009) A node-based smoothed finite element method (NS-FEM) for upper bound solutions to solid mechanics problems. *Comput Struct* 87:14–26
- [26] Liu GR, Nguyen-Thoi T, Lam KY (2009) An edge-based smoothed finite element method (ES-FEM) for static, free and forced vibration analyses of solids. *J Sound Vib* 320:1100–30
- [27] Nguyen-Thoi T, Liu GR, Lam KY, Zhang GY (2009) A face-based smoothed finite element method (FS-FEM) for 3D linear and geometrically non-linear solid mechanics problems using 4-node tetrahedral elements. *Int J Numer Methods Eng* 78:324–53
- [28] Nguyen-Thoi T, Liu GR (2011) Nguyen-Xuan H. An n-sided polygonal edge-based smoothed finite element method (nES-FEM) for solid mechanics. *Int J Numer Methods Biomed Eng* 27:1446–72
- [29] Nguyen-Xuan H, Liu GR, Bordas S, Natarajan S, Rabczuk T (2013) An adaptive singular ES-FEM for mechanics problems with singular field of arbitrary order. *Comput Methods Appl Mech Eng* 253:252–73
- [30] Liu F, Yu C, Yang Y (2018) An edge-based smoothed numerical manifold method and its application to static, free and forced vibration analyses. *Eng Anal Bound Elem* 86:19–30
- [31] Lee C, Lee PS (2018) A new strain smoothing method for triangular and tetrahedral finite elements. *Comput Methods Appl Mech Eng* 341:939–55
- [32] Lee C, Lee PS (2019) The strain-smoothed MITC3+ shell finite element. *Comput Struct* 223:106096
- [33] Lee C, Kim S, Lee PS (2021) The strain-smoothed 4-node quadrilateral finite element. *Comput Methods Appl Mech Eng* 373:113481
- [34] Lee C, Park J (2021) A variational framework for the strain-smoothed element method. *Comput Math with Appl* 94:76–93
- [35] Lien S, Kajiya JT (1984) A symbolic method for calculating the integral properties of arbitrary nonconvex polyhedra. *IEEE Comput Graph Appl* 4(10):35-42
- [36] Lee PS, Bathe KJ (2004) Development of MITC isotropic triangular shell finite elements. *Comput Struct* 82(11-12):945-962
- [37] Lee Y, Yoon K, Lee PS (2012) Improving the MITC3 shell finite element by using the Hellinger-Reissner principle. *Comput Struct* 110–111:93–106
- [38] Lee Y, Lee PS, Bathe KJ (2014) The MITC3+ shell element and its performance. *Comput Struct* 138:12–23

- [39] Timoshenko S, Goodier JN (1970) Theory of elasticity, 3rd ed. McGraw-Hill, New York
- [40] Liu CH, Hofstetter G, Mang HA (1994) 3D finite element analysis of rubber-like materials at finite strains. Eng Comput 11:111–128
- [41] Doll S, Hauptmann, Schweizerhof K, Freischlager C (1998) Selective reduced integration and volumetric locking in finite deformation elastoviscoplasticity. Institut für Mechanik, Universität Karlsruhe, Germany
- [42] Zienkiewicz OZ, Taylor RL (2000) The finite element method. 5th ed. Oxford, UK: Butterworth Heinemann
- [43] Liu GR (2009) Meshfree methods: moving beyond the finite element method. 2nd ed. Boca Raton: CRC Press
- [44] Li E, Zhang Z, Chang CC, Liu GR, Li Q (2015) Numerical homogenization for incompressible materials using selective smoothed finite element method. Compos Struct 123:216-232
- [45] JC Simo, F Armero (1992) Geometrically non-linear enhanced strain mixed methods and the method of incompatible modes. Int J Numer Methods Eng 33:1413-49
- [46] Hiller JF, Bathe KJ (2003) Measuring convergence of mixed finite element discretizations: An application to shell structures. Comput Struct 81:639–54.